*J. Fluid Mech.* (2001), *vol.* 447, *pp.* 53–84.  
DOI: 10.1017/S0022112001006073 Printed in the United Kingdom

# Large-eddy simulation of turbulent rotating convective flow development

By ANQING CUI AND ROBERT L. STREET

Environmental Fluid Mechanics Laboratory, Department of Civil and Environmental Engineering, Stanford University, Stanford, CA 94305-4020, USA

(Received 27 April 2000 and in revised form 9 May 2001)

Large-eddy simulations were carried out to simulate laboratory-scale isolated buoyant convection in unstratified water with shelf and slope topography in the presence of rotation and to compare and complement the experimental study of Jacobs & Ivey (1998) under the same conditions. The simulation code developed in this work was a three-dimensional incompressible Navier–Stokes solver and the simulation runs were performed on a distributed memory massively parallel computer, namely the IBM SP2, to study the effects of different applied heat fluxes and system rotation rates. We are able to show for the first time the detailed temporal evolution and spatial structure of the three-dimensional convective flow field. Rayleigh–Bénard instability in the form of circular concentric convective rings is recognized in the initiation process of the convection. The onset of Rayleigh–Bénard instability was investigated and the critical Rayleigh number was found to increase with Taylor number only when the Taylor number is greater than $5 \times 10^3$, where both non-dimensional parameters are based on the conductive layer thickness. The horizontally axisymmetric convective rings later break down and evolve into a quasi-two-dimensional vortex field. An azimuthal rim current develops around the periphery of the convective region. Our simulation results confirmed that the rim current velocity scales as $Bt^{1/2}/Hf^{3/2}$. Here $B$ is the buoyancy flux applied over a bottom circular disk, $f$ is the Coriolis parameter, $t$ is the time and $H$ is the distance between the tank bottom and the shelf. With increasing lateral temperature gradient the rim current undergoes a baroclinic instability. Our study of root-mean-square velocities in the convective region suggests that the transition from the buoyancy-flux-controlled to background-rotation-controlled flow occurred when the natural Rossby number $Ro^*$ became smaller than a critical value between 0.015 and 0.044. The simulation results of the convective overturning time, the wavelength of the baroclinic eddies and the density anomaly at steady state are all in reasonable agreement with the experimental data.

## 1. Introduction

Thermal convection in rotating fluids is important in many geophysical and engineering situations. Turbulent, rotating, convective flow arises when intense cooling at the ocean surface occurs in places such as the Gulf of Lions in the Mediterranean and some areas of the polar seas, namely the Greenland Sea, the Labrador Sea and the Weddell Sea. Turbulent convection in the open ocean plays a central part in determining global climate due to its role in the transport of surface water to deep locations and ultimately in the large-scale thermohaline circulations. Early work on deep ocean convection has been reviewed by Killworth (1983). More recent field

studies (Schott & Leaman 1991 and Schott, Visbeck & Fischer 1993) have reported direct observations of deep ocean convection events. However, there are very few observations of convective events which allow an identification of the structure and scales of the flow (Schott *et al.* 1993). Therefore, much of the understanding of the turbulent convection process continues to come from laboratory and numerical studies. During the past four decades, numerous analytical works, laboratory studies and numerical simulations have been performed on this subject.

The importance of rotation and its effect on the modelling of the relevant turbulent processes have been studied experimentally by Golitsyn (1981), Boubnov & Golitsyn (1986, 1990), Brickman (1995), Fernando, Boyer & Chen (1989), Fernando, Chen & Boyer (1991), Maxworthy & Narimousa (1994), Coates & Ivey (1993, 1997), Coates, Ivey & Taylor (1995), Narimousa (1997), and Jacobs & Ivey (1998, 1999). The laboratory investigations were supported by numerical modelling efforts. The numerical modelling study of deep ocean convection was initially done by Madec *et al.* (1991). They parameterized the convective processes and used a hydrostatic model to focus on the dynamics of the large-scale flow driven by the vertical convection. Since the turbulent convection process is non-hydrostatic by nature, numerical studies using non-hydrostatic models but constant eddy viscosity have been carried out by Brugge, Jones & Marshall (1991); Jones & Marshall (1993); Send & Marshall (1995); Sander, Wolf-Gladrow & Olbers (1995); Visbeck, Marshall & Jones (1996); Klinger, Marshall & Send (1996) and Denbo & Skyllingstad (1996). As Maxworthy & Narimousa (1994) point out, the choice of turbulent parameterization is critical in making quantitative comparison of numerical and laboratory models. Field-scale large-eddy simulation (LES) of non-hydrostatic models were performed by Raasch & Etling (1991); Garwood, Isakari & Gallacher (1994) and Noh, Jang & Kim (1999). In their studies, Raasch & Etling used a $k$–$\epsilon$ type eddy viscosity closure, while Noh *et al.* used a Smagorinsky eddy viscosity closure. In their simulations, the computational domain is in the 1.2 to 48 km range and the horizontal grid size is in the 20 to 250 m range. Legg & Marshall (1993) and Legg, Jones & Visbeck (1996) developed a point-vortex heton model and used it to study localized ocean convection.

The two common difficulties with previous LES studies are insufficient grid resolution and inadequate turbulence models. The advent of massively parallel processing and the extensive efforts that have been put into the development of new large-eddy simulation models provide the possibility of performing large-scale computations of turbulent flows for complex geometries. Since three-dimensional numerical simulations reproduce many important characteristics of turbulent flows and allow one to extract information which cannot be easily obtained from laboratory experiments or field observations, the objective of this study was to conduct a large-eddy simulation to compare with and to complement the experimental study of Jacobs & Ivey (1998) in investigating the fundamental mechanisms of a turbulent rotating convective flow. The two fundamental features of our work are: (i) an extensive grid resolution study leading to resolution of all important features of the flow field and (ii) implementation of a subgrid-scale turbulence model in the LES that is known to properly characterize the flow (Zang, Street & Koseff 1993; Salvetti & Banerjee 1995 and Piomelli 1999).

In the course of the grid study, we realized that the early stage of the convective flow in this study relates to Rayleigh–Bénard convection, which was not the focus of Jacobs & Ivey's (1998) experimental study. Rayleigh–Bénard convection has been the subject of numerous analytical and experimental studies. In 1900, Bénard performed the first systematic experimental investigation of convection in a shallow fluid layer heated from below. The basic theoretical study of convection caused by heating from

below was pioneered by Rayleigh (1916). The topic of the onset of thermal instability in horizontal layers of fluid heated from below with and without rotation about a vertical axis is discussed in the second and third chapters of Chandrasekhar (1961). Some laboratory studies of rotating Rayleigh–Bénard convection have been done by Nakagawa & Frenzen (1955), Koschmieder (1966) and Rossby (1969). Then, for about three decades, the experimental studies were mostly neglected until Boubnov and Golitsyn started a series of systematic experimental studies of the convection in a horizontal convective layer (see Boubnov & Golitsyn 1986, 1990).

Two recent books by Koschmieder (1993) and Boubnov & Golitsyn (1995) describe the impressive progress that has been made in the theoretical and experimental investigations of Rayleigh–Bénard convection and convection in rotating fluid. Three-dimensional numerical simulations of Bénard-like convection in a rotating frame have been performed by Somerville & Lipps (1973) and Hathaway & Somerville (1983). A direct numerical simulation of laminar and turbulent Benard convection with $64 \times 32^2$ grid points has been done by Grötzbach (1982). To the authors knowledge, no numerical simulation work has been devoted to studying the critical values of onset of Rayleigh–Bénard instability, such as the critical Rayleigh number, the number of rings formed, etc. One possible reason is the large number of grid points needed in the simulation to resolve the small-scale flow structures. Since the corresponding experimental study of Jacobs & Ivey (1998) did not study the early stage of their rotating convective flow and no theoretical results can be directly applied to their flow, it is worth studying some questions, such as the rotation effect on the critical Rayleigh number, the time of the formation of the convective rings and the number of rings formed, etc., with our simulation effort. Because deep convection in the ocean is usually a transient phenomenon, our simulation can provide insight into the development of the turbulent rotating convective flow there.

The remainder of the paper is organized as follows. The flow configuration used in the simulations is described in § 2. The governing equations, numerical method and the initial and boundary conditions for the simulations are presented in § 3. The simulation results are presented in § 4. Conclusions are given in § 5.

## 2. Flow configuration

Large-eddy simulations are carried out in the present study to complement an experimental study of Jacobs & Ivey (1998). Their laboratory-scale experiments were conducted at the University of Western Australia to model the turbulent convection processes in an ocean driven by the energetic cooling at the ocean surface. In their experiment, the flow was inverted for experimental convenience so that heating at the bottom is used to drive the convective, rotating flow. All the experiments were conducted using water. Figure 1 is a schematic of the cross-section of the experimental apparatus. The experiments were conducted in a circular Perspex tank of radius $R_o = 0.48$ m. The circular tank was surrounded by a slightly larger outer tank, with the volume between the two tank walls filled with water at the same temperature as the water in the working section. The tank was fitted with a false bottom with built-in circular copper plate of radius $R_i = 0.2$ m that acted as a heat exchanger. The copper plate formed the upper surface of a heat exchanger and could be heated by pumping hot fluid from a constant temperature bath through a circuit of pipes built into the copper plate. The plate was insulated on the sides and the bottom, so that heat could only escape through the top surface. The heat flux $Q$ was determined by measurements of the volume flow rates and temperature drop of the heated fluid

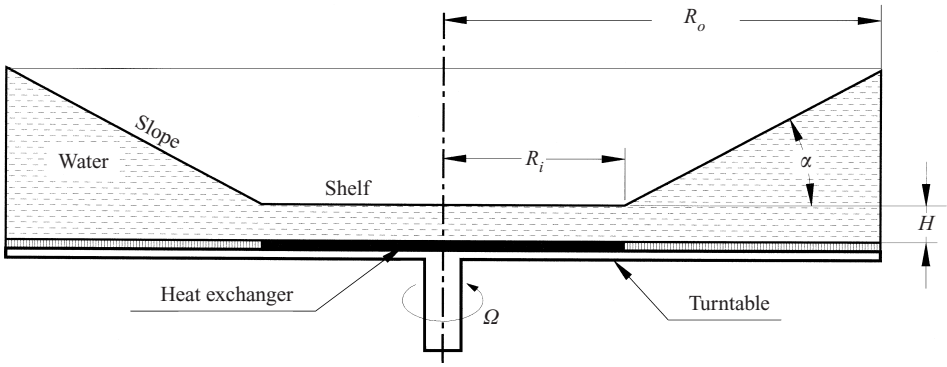


FIGURE 1. A schematic of the cross-section of the experimental apparatus.

passing through the heat exchanger. According to Jacobs & Ivey (1998), the heat flux $Q$ could be determined with an accuracy of about 6%, and errors in the values of buoyancy flux are up to 10%. The tank top was closed with a model of a shelf and slope with an angle $\alpha = 28^\circ$ commencing at the same radius as the edge of the heated area. The top lid consists of a cellular Perspex construction with air sealed in the interior, which is an adequate insulator. The distance $H$ between the tank bottom and the shelf was varied between experiments and had values of 0.04 m and 0.08 m. The entire assembly was mounted on a rotating table, revolving counter-clockwise about the vertical axis at a constant rate $\Omega$. Details of the experimental apparatus can be found in Jacobs & Ivey (1998). The flow configuration in present simulation is exactly the same as their experiment except that a small cylinder of 0.02 m radius ($R_h$) was cut from the numerical domain to eliminate the coordinate singularity at the centre for the numerical simulation.

## 3. Governing equations and numerical method

### 3.1. *Governing equations*

The governing equations in the present study are the grid-filtered continuity, Navier–Stokes and scalar transport equations under the Boussinesq approximation:

$$\frac{\partial \bar{u}_j}{\partial x_j} = 0, \tag{3.1}$$

$$\frac{\partial \bar{u}_i}{\partial t} + \frac{\partial \bar{F}_{ij}}{\partial x_j} = \bar{S}_i, \tag{3.2}$$

$$\frac{\partial \bar{T}}{\partial t} + \frac{\partial \bar{R}_j}{\partial x_j} = 0, \tag{3.3}$$

where

$$\bar{F}_{ij} = \bar{u}_i\bar{u}_j + \bar{p}\delta_{ij} - \nu\frac{\partial \bar{u}_i}{\partial \bar{x}_j} + \tau_{ij}, \tag{3.4}$$

$$\bar{S}_i = -g\beta(\bar{T} - T_0)\delta_{i2} + f(-\bar{u}_3\delta_{i1} + \bar{u}_1\delta_{i3}) + \Omega^2(x_i - \delta_{i2}x_2), \tag{3.5}$$

$$\bar{R}_j = \bar{u}_j\bar{T} - \kappa\frac{\partial \bar{T}}{\partial x_j} + \chi_j. \tag{3.6}$$

In the above equations, a variable with an overbar indicates a grid-filtered quantity, $t$ is the time, $u_i$ ($i = 1, 2, 3$) are the Cartesian velocity components in the directions $(x_1, x_2, x_3)$, where $x_1$ and $x_3$ are the horizontal coordinates and $x_2$ is the upward vertical direction, $\bar{p}$ is the pressure, $g$ is the gravitational constant, $\Omega$ is the system rotation rate, $f = 2\Omega$ is the Coriolis parameter, $T$ is the temperature, $T_0$ is a reference temperature, $\beta$ is the thermal expansion coefficient, and $\nu (= 10^{-6}\,\mathrm{m^2\,s^{-1}})$ and $\kappa$ represent, respectively, the kinematic viscosity and thermal diffusivity of the fluid. The ratio $\nu/\kappa$ is the Prandtl number $Pr$, which is equal to 7 in this work where water is the working fluid. The Einstein summation rule applies to all the terms of the above equations.

The filtered governing equations (3.2) and (3.3) contain subgrid-scale terms $\tau_{ij}$ and $\chi_j$, which are defined as

$$\tau_{ij} = \overline{u_i u_j} - \bar{u}_i \bar{u}_j, \tag{3.7}$$

$$\chi_j = \overline{u_j T} - \bar{u}_j \bar{T}. \tag{3.8}$$

These two subgrid-scale quantities are modelled using the dynamic mixed subgrid-scale model described in Zang *et al.* (1993), which is able to calculate the model coefficient locally using the resolved quantities by filtering the governing equations at two different spatial scales. A local averaging together with a cutoff are used to prevent numerical instability. Details of filtering and cutoff criteria can be found in Zang *et al.* (1993). To test the turbulence model, large-eddy simulations of three-dimensional isothermal lid-driven cavity flows were carried out to compare with the experimental study of Prasad & Koseff (1989). The simulation results compare well with experimentally measured mean, r.m.s. velocity and Reynolds stress profiles in both the laminar and turbulent flows. In LES the contribution of the large, energy-carrying structures to momentum and energy transfer is simulated accurately, and only the effect of the smallest scales of turbulence is modelled. In other words, in LES the turbulence model only plays a role in places where there are not enough grid points in the simulation to resolve the smallest scale of the flow. By analysing the energy dissipation ratio of subgrid-scale dissipation to viscous dissipation in the rotating convective flow simulation, Cui (1999) demonstrated that the subgrid-scale dissipation represents only a minor fraction of the total dissipation. Therefore, the role of the subgrid-scale model is small in this work due to the large number of grid points used in the present simulation.

### 3.2. *Numerical method*

The governing equations are transformed into a generalized coordinate system and discretized using a finite-volume formulation on a single non-staggered grid. The equations are discretized in time with a semi-implicit scheme with the Crank–Nicholson method for the diagonal viscous and diffusive terms and the Adams–Bashforth method for all the other terms. All the spatial derivatives are approximated with second-order central differences with the exception of the convective terms, which are handled with accurate upwind-difference schemes. The convective terms in the momentum equation are discretized using QUICK (Leonard 1979) and the convective term in the scalar transport equation is discretized using SHARP (Leonard 1988).

The fractional-step, non-staggered solution technique of Zang, Street & Koseff (1994) is used to advance the discretized equations in time. An estimate of the velocity field is obtained with a third-order-accurate factorization by solving the momentum equation with the pressure term omitted. Continuity is then enforced by solving a pressure Poisson equation with a multi-grid method. Zang *et al.* (1994),

| Case | Grid ($N_r \times N_y \times N_\theta$) | $\Omega$(rad s$^{-1}$) | $B \times 10^6$(m$^2$ s$^{-3}$) | $Ro^*$ |
|---|---|---|---|---|
| Run 1 | $352 \times 128 \times 256$ | 0.2 | 1.57 | 0.124 |
| Run 2 | $352 \times 128 \times 256$ | 0.0 | 1.57 | 0.124 |
| Run 3 | $352 \times 128 \times 256$ | 0.1 | 1.57 | 0.350 |
| Run 4 | $352 \times 128 \times 256$ | 0.4 | 1.57 | 0.044 |
| Run 5 | $352 \times 128 \times 256$ | 0.8 | 1.57 | 0.015 |
| Run 6 | $352 \times 128 \times 256$ | 0.2 | 3.14 | 0.175 |

TABLE 1. Grid resolutions and physical parameters of the simulations.

Zang & Street (1995) and Yuan, Street & Ferziger (1999) showed the quantitative accuracy of the numerical schemes for laboratory scale simulations.

The numerical code was implemented on a distributed-memory, massively-parallel computer – the IBM SP2, using the message passing interface (MPI). Details of the code implementation can be found in Cui & Street (2000). A code performance of 38 MFLOPS per node was achieved, which was the reported peak rate in a retrospective study of codes run on the IBM SP2 at NASA-Ames during a eight-month period (Bergeron 1998). This parallel code has been validated against a variety of laboratory-scale flows (Cui 1999), such as lid-driven cavity flow, upwelling flows and flows induced by source–sink pairs in a rotating stratified fluid.

### 3.3. *Initial and boundary conditions*

The working fluid, i.e. pure water, is initially at a uniform temperature $T_i$ and is in solid-body rotation with the tank. At time $t = 0$, a constant and uniform heat flux $Q$ is applied to the bottom central disk. No-slip velocity boundary conditions are imposed at all solid walls. Except at the bottom central disk, where a constant and uniform heat flux $Q$ is applied, the temperature boundary conditions for the inner vertical wall, the top lid and the bottom of the tank are obtained by assuming that those walls are adiabatic. A constant temperature, equal to the initial temperature $T_i$, is applied to the outer vertical wall. The buoyancy flux $B$ can be related to the heat flux $Q$ through $B = g\beta Q/(\rho C_p)$, with the thermal expansion coefficient $\beta = 2.5 \times 10^{-4} \,^\circ\mathrm{C}^{-1}$, the gravitational acceleration constant $g = 9.81\,\mathrm{m\,s^{-2}}$, the density $\rho = 1000\,\mathrm{kg\,m^{-3}}$ and the specific heat at constant pressure $C_p = 4180\,\mathrm{J\,kg^{-1}\,K^{-1}}$.

## 4. Simulation results

To investigate the effect of rotation and heating on the convection process, a total of six production runs were performed covering five different angular velocities $\Omega$ and two different buoyancy fluxes $B$ while the geometric parameters were fixed. An extensive grid resolution study was conducted (Cui 1999) and led to the use of up to twelve million grid points in the simulation. A summary of the grid resolutions and physical parameters for our study is given in table 1. $Ro^*$ in table 1 is the natural Rossby number introduced by Golitsyn (1980) as $Ro^* = [B/(f^3H^2)]^{1/2}$, which is the ratio of the rotation time scale to the time scale for turnover of a fully turbulent convective eddy in a fluid of depth $H$. Run 1 has the same physical parameters as experiment number 14 of Jacobs & Ivey's (1998) experiment. The only difference among Run 1 to Run 5 is the angular velocity $\Omega$, which is varied from 0 to 0.8 rad s$^{-1}$. The difference between Run 1 and Run 6 is that the buoyancy flux $B$ of Run 6 is twice that of Run 1.

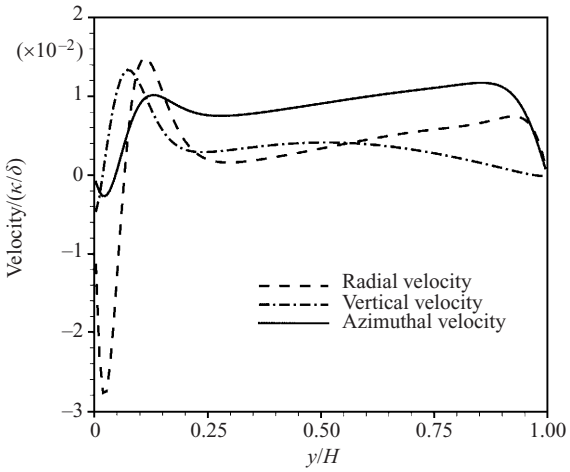


FIGURE 2. Velocity profiles at $r/R_i = 0.5$ and $t = 28$ s (Run 1).

In order to resolve the small-scale flow structures inside the convective region, a non-uniform grid is used in the radial direction with grid points clustered in the constant-height shelf region and then stretching out radially. The grid is uniform in the vertical and the azimuthal directions. Since the viscous stability limit is removed by advancing the diagonal viscous terms implicitly, the time step $\Delta t$ is then determined by the Courant–Friedrichs–Lewy (CFL) number

$$\mathrm{CFL} = \left( \frac{|u_1|}{\Delta x} + \frac{|u_2|}{\Delta y} + \frac{|u_3|}{\Delta z} \right) \Delta t, \tag{4.1}$$

where $\Delta x, \Delta y, \Delta z$ are the grid spacings in the three Cartesian coordinates in the physical domain. The stability condition of the present method requires the maximum value of the CFL number obtained from (4.1) over the entire computational domain to be less than one. A fixed time step $\Delta t = 0.02$ s was used so that the CFL number was always less than 0.75 in our simulation. A step-by-step description of the convection process is given below. In presenting the results, we employ a right-handed $(x, y, z)$ system with $y$ being the vertical distance up from the plate. In addition, $r = \sqrt{x^2 + z^2}$ is the radial coordinate in the horizontal $(x, z)$-plane.

### 4.1. *Growth of the conductive layer*

The water is at a uniform temperature $T_i$ and is initially in solid-body rotation with the tank. At time $t = 0$, a constant and uniform buoyancy flux $B$ is applied to the bottom central disk. A thin thermal layer then forms immediately above the heat source and grows diffusively with time. The thin thermal layer grows uniformly in the vertical direction except at the outer edge of the heated disk. Due to the discontinuity of the heat flux applied at the bottom of the tank, some radial momentum and heat exchanges take place at the outer edge of the heated disk. In figure 2, the velocity profiles, which are non-dimensionalized by a velocity scale $V$ = (thermal diffusivity $\kappa$)/(thermal layer thickness $\delta$), indicate that all the three velocity components are negligibly small within the thermal layer and, therefore, that a basic static state of heat conduction exists. (Note that the actual velocity at the sidewall is zero, but that is not a node point and is not plotted.) Since molecular conduction dominates inside this thermal layer, we call it *the conductive layer*. Temperature profiles in figure 3 show that the

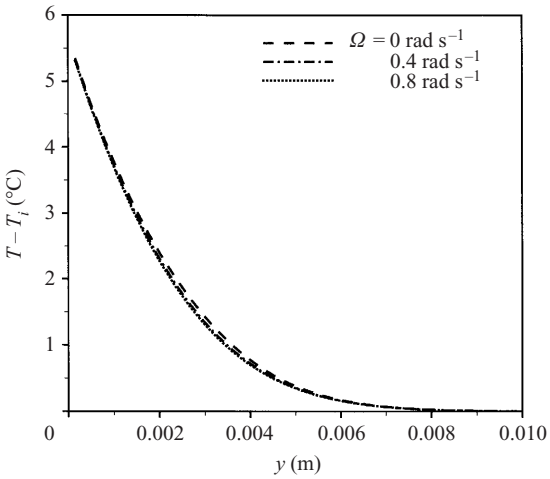


FIGURE 3. Temperature profiles at $r/R_i = 0.5$ and $t = 35$ s for different angular velocities $\Omega$ (Runs 1, 2 and 5).

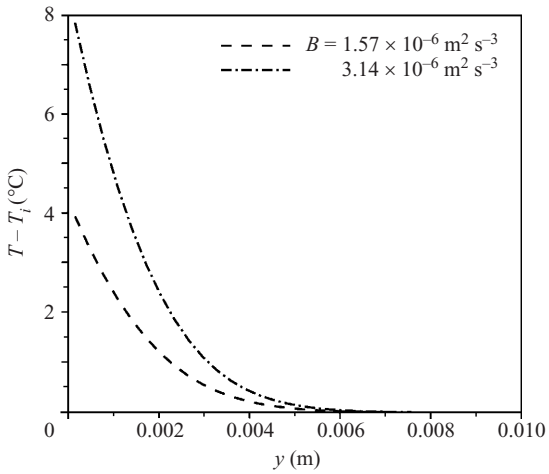


FIGURE 4. Temperature profiles at $r/R_i = 0.5$ and $t = 20$ s for different buoyancy fluxes $B$ (Run 1 and Run 6).

angular velocity $\Omega$ has no effect on the growth of the conductive layer. In addition, temperature profiles for different buoyancy fluxes $B$ at $t = 20$ s presented in figure 4 show that the conductive layer thickness does not depend on the buoyancy flux $B$. Based on the unsteady one-dimensional heat conduction equation, a dimensionally correct scale for the conductive layer thickness $\delta(t)$ can be introduced as

$$\delta(t) \sim \sqrt{\kappa t}, \tag{4.2}$$

where $\kappa$ is the thermal diffusivity and $t$ is the time. The temperature profiles for Run 1 at different times plotted against the non-dimensionalized vertical distance $y/\sqrt{\kappa t}$ are shown in figure 5. All the curves approach the same non-dimensional thickness value, suggesting that $\sqrt{\kappa t}$ is the correct length scale for the conductive layer thickness.

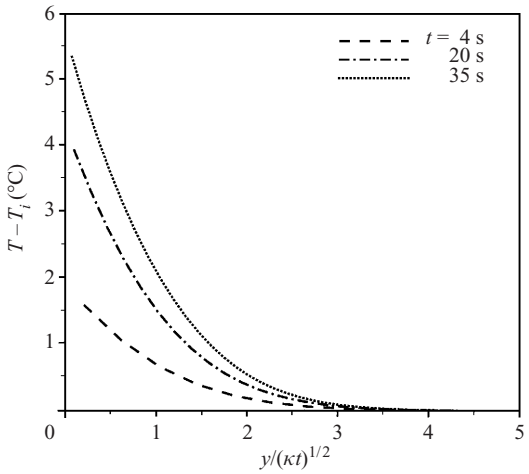


FIGURE 5. Temperature profiles at $r/R_i = 0.5$ and different times (Run 1).

### 4.2. *Onset of the Rayleigh–Bénard convection*

The temperature difference across the conductive layer increases as the layer thickness increases. When the temperature difference exceeds a critical value $\Delta T_c$, the buoyancy of the fluid is able to overcome the dissipation caused by the viscosity and thermal diffusivity of the fluid, the basic static state becomes unstable and the convective instability, i.e. the Rayleigh–Bénard convection, sets in. The Rayleigh number $Ra_\delta$ is a non-dimensional measure of the vertical temperature difference across the layer that is necessary to overcome the dissipative influences of viscosity and heat conduction; $Ra_\delta$ is given by

$$Ra_\delta = g\beta\Delta T\delta^3/(\nu\kappa). \tag{4.3}$$

The Taylor number $Ta_\delta$ is a non-dimensional measure of the rotation rate of a fluid layer rotating with angular velocity $\Omega$; $Ta_\delta$ is defined as

$$Ta_\delta = 4\Omega^2\delta^4/\nu^2. \tag{4.4}$$

The conductive layer thickness $\delta$, instead of the distance $H$ between the tank bottom and the shelf, is used here since a fluid particle has travelled only within the distance $\delta$ when Rayleigh–Bénard convection takes place. The onset of the Rayleigh–Bénard convection can be observed through the formation of circular concentric convective rings (figure 6). Jacobs & Ivey (1998) did not study the onset of the Rayleigh–Bénard convection. However, the existence of the convective rings above a uniformly heated circular plate was observed in experiments reported by Koschmieder (1966) and Boubnov & Golitsyn (1986). Expanded side views of the velocity and temperature fields† (figure 7) shows the warm water trapped in the convective rings rising from the bottom heat source and the cold water descending between them.

Table 2 tabulates the values of the time $t$, the critical temperature difference $\Delta T_c$, the corresponding critical Rayleigh number $Ra_c$, the layer thickness $\delta$ and Taylor number $Ta_\delta$ when the onset of Rayleigh–Bénard convection occurs for different runs.

† All the side view velocity plots in this paper are plotted at every third point in the radial direction, at every seventh point in the vertical direction. All the temperature plots in this paper show the temperature deviation from the initial temperature.

| Case | $t$ (s) | $\Delta T_c$ (°C) | $\delta$ (mm) | $Ra_c \times 10^4$ | $Ta_\delta$ |
|---|---|---|---|---|---|
| Run 1 | 35 | 5.3 | 7.1 | 7.1 | $1.1 \times 10^3$ |
| Run 2 | 35 | 5.3 | 7.1 | 7.1 | $0.0 \times 10^3$ |
| Run 3 | 35 | 5.3 | 7.1 | 7.1 | $0.3 \times 10^3$ |
| Run 4 | 35 | 5.3 | 7.1 | 7.1 | $4.6 \times 10^3$ |
| Run 5 | 38 | 5.7 | 9.2 | 8.2 | $2.1 \times 10^4$ |
| Run 6 | 23 | 8.5 | 7.7 | 6.9 | $1.1 \times 10^3$ |

TABLE 2. Values observed at the onset of Rayleigh–Bénard convection.

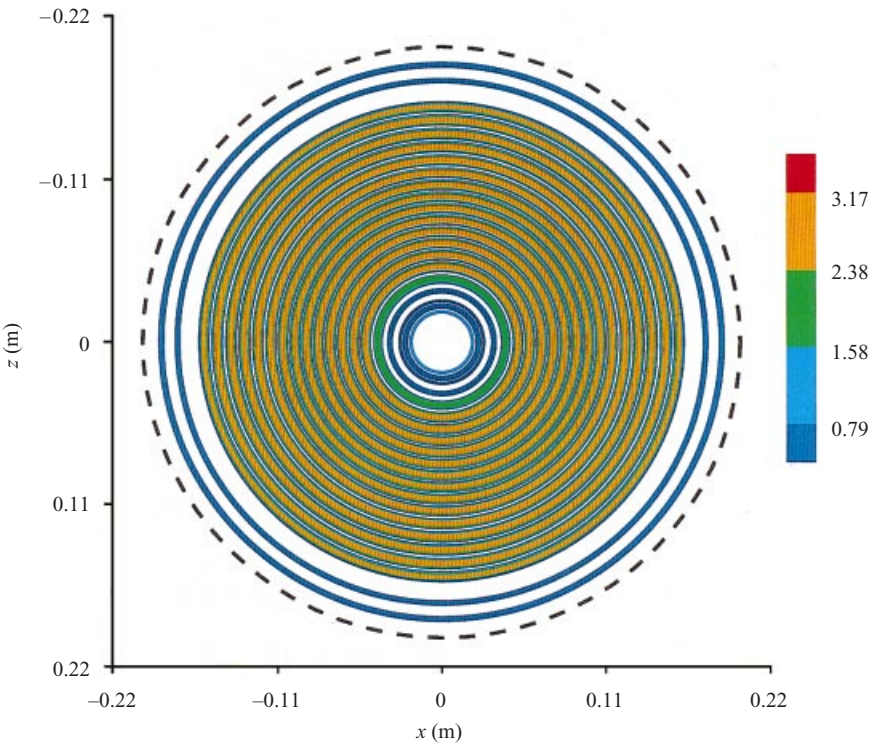


FIGURE 6. Plan view of the temperature field at $t = 40\,\mathrm{s}$ and $y/H = 0.125$ for $\Omega = 0.2\,\mathrm{rad\,s^{-1}}$, $B = 1.57 \times 10^{-6}\,\mathrm{m^2\,s^{-3}}$ (Run 1). The rim of the heated disk is marked by the dashed line.

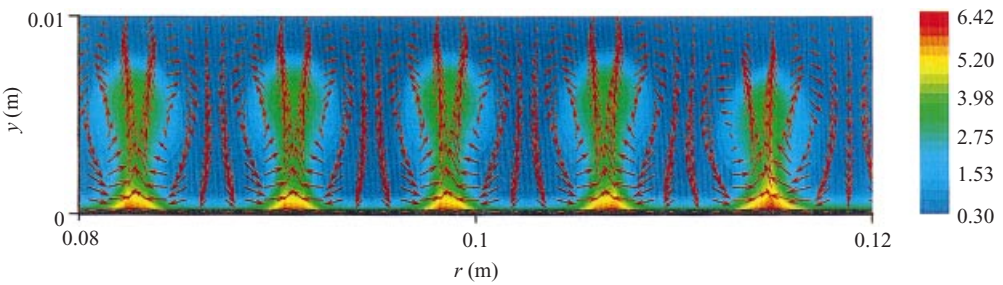


FIGURE 7. Expanded side view of the temperature and velocity fields at $t = 40\,\mathrm{s}$ for $\Omega = 0.2\,\mathrm{rad\,s^{-1}}$, $B = 1.57 \times 10^{-6}\,\mathrm{m^2\,s^{-3}}$ (Run 6).

From table 2, the following conclusions can be drawn:
(i) The time for the formation of the convective rings depends on the supplied buoyancy flux $B$. It does not depend on the rotation rate $\Omega$ when $Ta_\delta < 5 \times 10^3$ and begins to increase when $Ta_\delta > 5 \times 10^3$ when the other external conditions remain the same.
(ii) The critical Rayleigh number $Ra_c$ is essentially constant ($Ra_c \approx 7 \times 10^4$) when $Ta_\delta < 5 \times 10^3$ and begins to increase with $Ta_\delta$ as $Ta_\delta > 5 \times 10^3$.

Analytical solutions for three combinations of boundary conditions on the bounding horizontal planes, i.e. the cases of two free boundaries, two rigid boundaries, and one rigid and one free boundary, are available for the thermal instability of a layer of fluid heated from below with or without rotation (Chandrasekhar 1961). The book by Boubnov & Golitsyn (1995) provides the critical Rayleigh number for an additional six boundary condition sets. Without rotation, the critical Rayleigh number $Ra_c$ is found to be a different constant for different boundary conditions. Under the effect of rotation, $Ra_c$ increases with the Taylor number $Ta_\delta$ when $Ta_\delta$ is greater than $10^3$. When $Ta_\delta$ is less than $10^3$, the dependence of $Ra_c$ on $Ta_\delta$ is not significant. The present numerical study differs from the analytical work in the following respects:
(i) The boundary conditions imposed on the horizontal planes of the present study do not fall into any of the nine types of the boundary conditions in the analytical work.
(ii) In the analytical work, a steady adverse temperature gradient is maintained within an infinite horizontal layer of fluid. The present numerical results (figure 5) show clearly an unsteady, nonlinear temperature distribution within the conductive layer.

Although the numerical result cannot be compared to the analytical result quantitatively, the analytical results may serve as a guide to the numerical results. The finding that the critical Rayleigh number $Ra_c$ is essentially constant when $Ta_\delta < 5 \times 10^3$ and increases with $Ta_\delta$ when $Ta_\delta > 5 \times 10^3$ is consistent with the analytical solutions.

### 4.3. *Development of the convective rings*

The *convective ring development* stage in this study refers to the process from the initial formation of the convective rings near the bottom of the tank to their arrival at the top shelf. Figures 6, 7 and 8 show the early stage of the convective rings, where they are mostly uniform. The non-uniformity of the ring patterns near the inner and outer edges is caused by the adiabatic wall condition and by the discontinuity of heat flux at the tank bottom, respectively.

In terms of the number of rings observed for different rotation rates and buoyancy fluxes, it is only reasonable to make comparisons within a region not under the direct influence of the edges of the heated disk. A distinct ring pattern can be seen for the radius range from 0.05 m to 0.17 m from figures 8(*a*) to 8(*d*). Within that radius range, the number of rings observed remains 16 (figures 8*a* and 8*b*) for the first four cases with the rotation rate increased from 0 to 0.4 rad s$^{-1}$. As the heat flux or the rotation rate further increased (or the Taylor number increased), the number of rings also increased. Figures 8(*c*) and 8(*d*) show 17 rings within the radius range from 0.05 m to 0.17 m. The above simulation results lead us to reach the following conclusions: (i) the number of rings formed depends on the buoyancy flux and (ii) the number of rings starts to increase when $Ta_\delta > 5 \times 10^3$. The critical wavelength $\lambda_c$ is the width of the layer divided by the number of rings when the critical Rayleigh number $Ra_c$

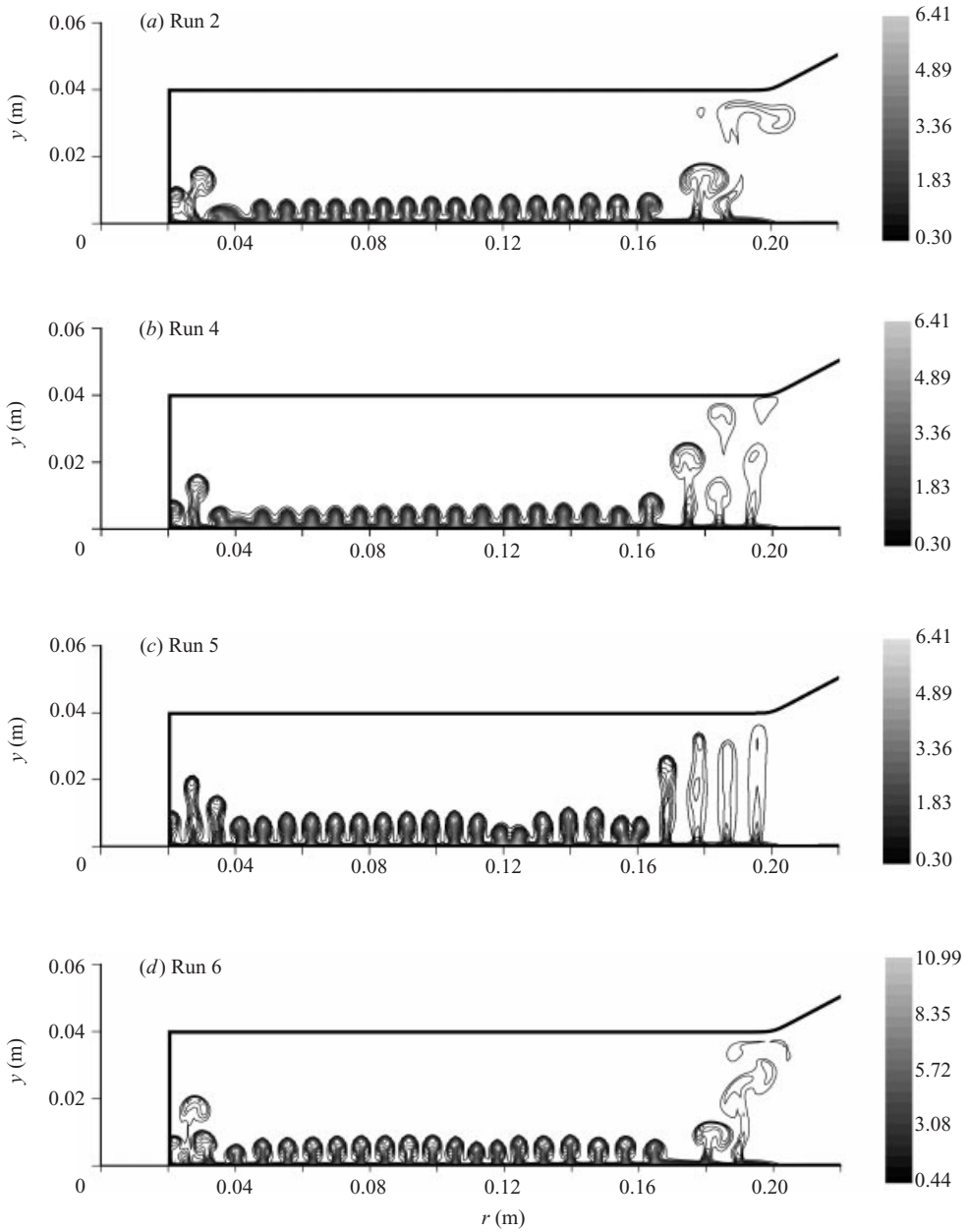


FIGURE 8. Side view of the temperature field. (*a*) $t = 40\,\mathrm{s}$ for Run 2 ($\Omega = 0.0\,\mathrm{rad\,s^{-1}}$, $B = 1.57 \times 10^{-6}\,\mathrm{m^2\,s^{-3}}$); (*b*) $t = 40\,\mathrm{s}$ for Run 4 ($\Omega = 0.4\,\mathrm{rad\,s^{-1}}$, $B = 1.57 \times 10^{-6}\,\mathrm{m^2\,s^{-3}}$); (*c*) $t = 45\,\mathrm{s}$ for Run 5 ($\Omega = 0.8\,\mathrm{rad\,s^{-1}}$, $B = 1.57 \times 10^{-6}\,\mathrm{m^2\,s^{-3}}$); (*d*) $t = 30\,\mathrm{s}$ for Run 6 ($\Omega = 0.2\,\mathrm{rad\,s^{-1}}$, $B = 3.14 \times 10^{-6}\,\mathrm{m^2\,s^{-3}}$).

occurs. As pointed out by Koschmieder (1993), little work has been devoted to the measurement of the critical wavelength $\lambda_c$ (therefore the number of rings) although $\lambda_c$ is a fundamental feature of Rayleigh–Bénard convection. Boubnov & Golitsyn (1986) reported that the distance between the rings ($r$) may vary by 50% in their experiment even when their experiments were repeated with exactly the same external

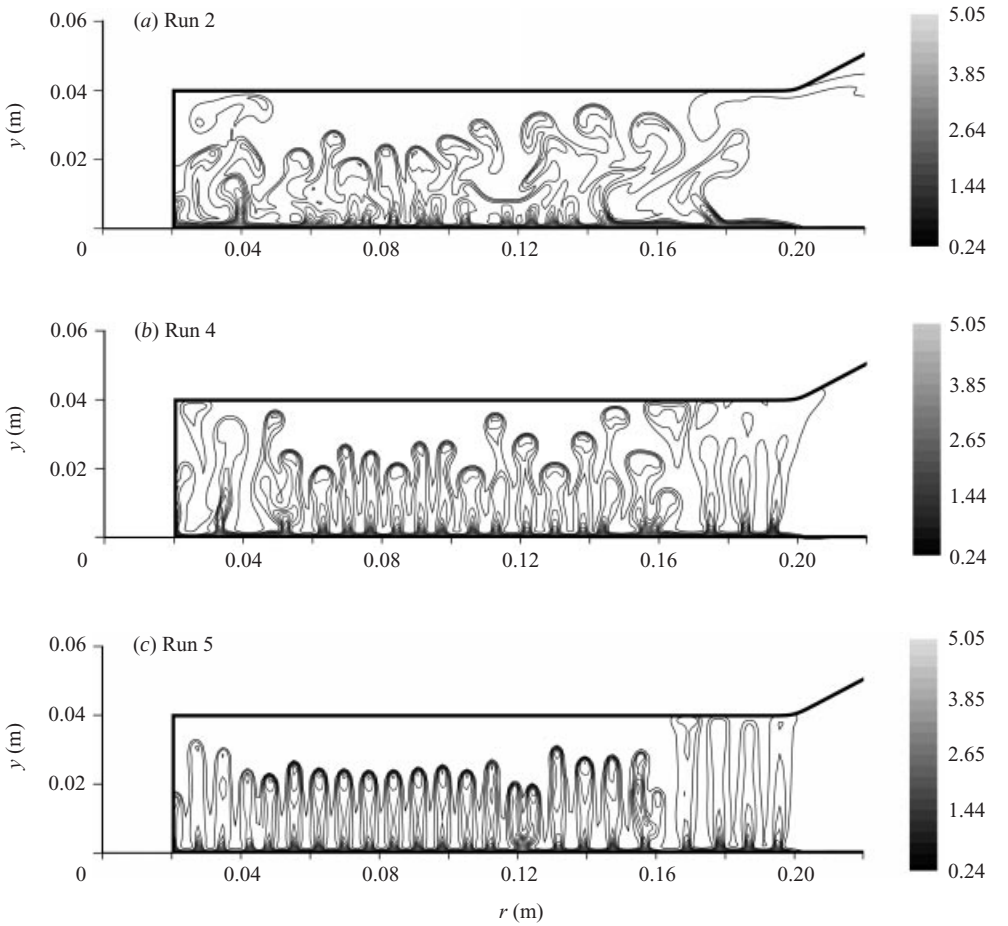


FIGURE 9. Side view of the temperature field. (*a*) $t = 55\,\mathrm{s}$ for Run 2 ($\Omega = 0.0\,\mathrm{rad\,s^{-1}}$, $B = 1.57 \times 10^{-6}\,\mathrm{m^2\,s^{-3}}$); (*b*) $t = 55\,\mathrm{s}$ for Run 4 ($\Omega = 0.4\,\mathrm{rad\,s^{-1}}$, $B = 1.57 \times 10^{-6}\,\mathrm{m^2\,s^{-3}}$); (*c*) $t = 55\,\mathrm{s}$ for Run 5 ($\Omega = 0.8\,\mathrm{rad\,s^{-1}}$, $B = 1.57 \times 10^{-6}\,\mathrm{m^2\,s^{-3}}$).

parameters. They also found that there was a clear dependence of $r$ on the heat flux, but no dependence on the rotation rate. However, Koschmieder (1967) found that the number of rings starts to increase with $Ta_\delta$ when $Ta_\delta > 10^5$ in their experiment. Because the experiment carried out by Jacobs & Ivey (1998) did not focus on the early stages of the convection process, no comparison regarding the number of rings can be made at this point. However, Ivey (2000, personal communication) advised us that the video and still pictures obtained from their experiments suggest the existence of ring patterns for a short time period.

By $t = 55\,\mathrm{s}$, the continuing penetration of the rings is evident, and some of them have already reached the top shelf (figures 9*a* to 9*c*). The simulation results in figure 9 show that the horizontal motions are directly affected by the rotation rate. The horizontal velocity components are more restrained with increasing rotation rate, and the lateral temperature difference increases near the edges of the heat source with increasing buoyancy flux; therefore the radial momentum and heat exchanges near the edges of the heated disk are different for the system under different rotation rates and subjected to different buoyancy fluxes. As a direct result, temperature distributions

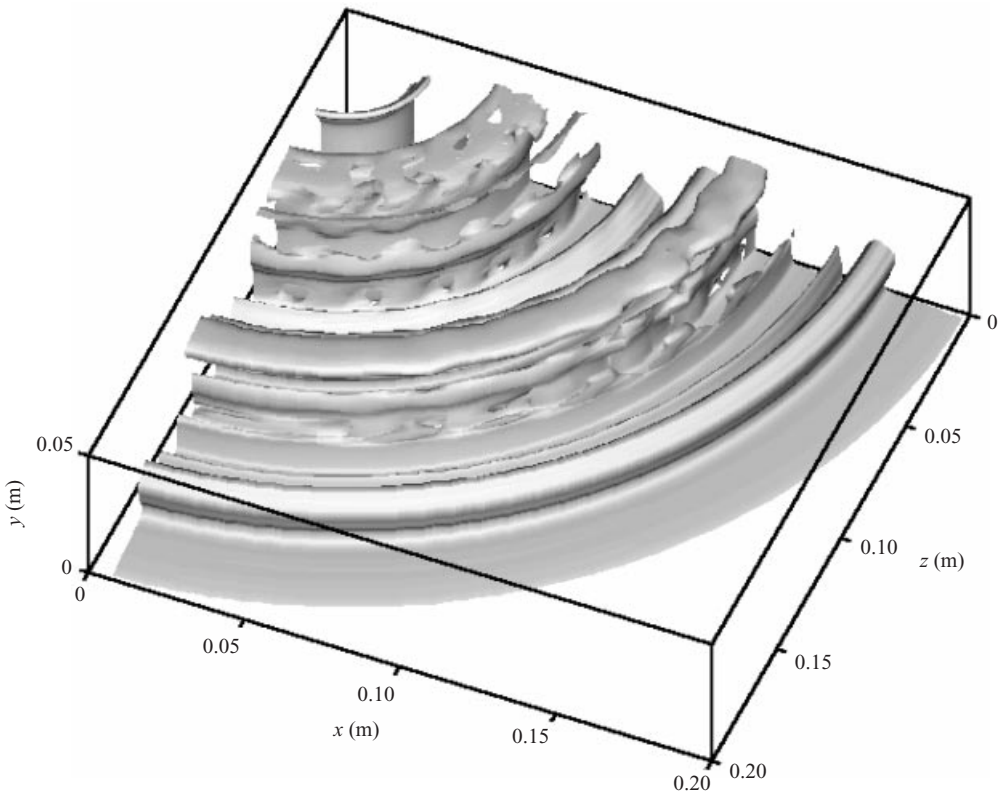


FIGURE 10. An iso-thermal surface at $t = 140\,\mathrm{s}$ for $\Omega = 0.2\,\mathrm{rad\,s^{-1}}$, $B = 1.57 \times 10^{-6}\,\mathrm{m^2\,s^{-3}}$ (Run 1).

near the edges of the heated disk are different from early in the simulation (figures 8*a* to 8*d*). The rings are more deformed in the vertical direction with the decrease of the angular velocity $\Omega$, resulting in a radially irregular ring pattern. Some blobs of warm water have already been detached from the rings by $t = 55\,\mathrm{s}$ at lower angular velocities (figure 9*a*). Despite the non-uniform pattern in the vertical and radial directions, the rings are still axisymmetric in the azimuthal direction.

A comparison of results at $t = 55\,\mathrm{s}$ for different rotation rates (figures 9*a* to 9*c*) shows that rotation has little effect on the time it takes for the rings to reach the top shelf, suggesting that the time scale for the ring development stage is approximately independent of the angular velocity $\Omega$. The present simulation results show that increasing the buoyancy flux reduces the time for the rings to reach the top shelf; for example, for Run 6 the time is about 40 s. As suggested by Jacobs & Ivey (1998), the time scale characterizing the convective ring development stage is given by the time it takes for a fluid particle with a typical vertical convective velocity $(BH)^{1/3}$ to travel over the vertical length scale $H$:

$$t_v \sim H/(BH)^{1/3} = (H^2/B)^{1/3}. \tag{4.5}$$

From table 2, one can see that the time of the onset of the convective instability for Run 5 is slightly different from that of Run 1 and Run 4 even though Run 1 to Run 5 have the same buoyancy flux ($B$), suggesting a possible rotation rate influence. However, our results show that it takes about the same time for the rings to reach the same vertical level in Run 1 to Run 5 after the onset of the instability. By observation

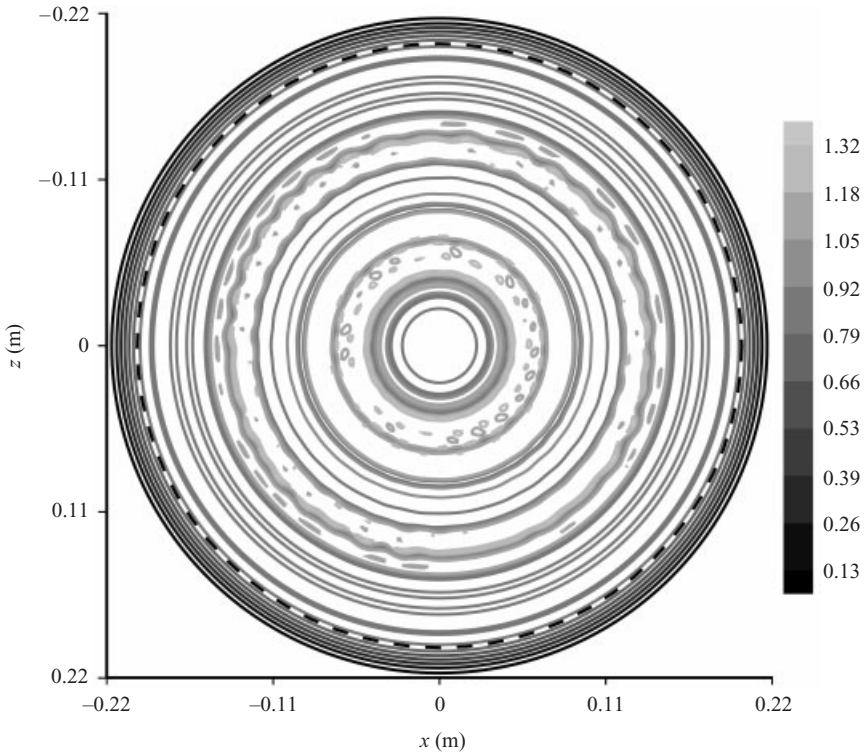


FIGURE 11. Plan view of the temperature field at $t = 140\,\mathrm{s}$ and $y/H = 0.5$ for $\Omega = 0.2\,\mathrm{rad\,s^{-1}}$, $B = 1.57 \times 10^{-6}\,\mathrm{m^2\,s^{-3}}$ (Run 1). The rim of the heated disk is marked by the dashed line.

of the time near the end of the ring development stage for Run 1 and Run 6, the ratio of the two time scales ($t_{v-Run1}$ for Run 1 to Run 5 and $t_{v-Run6}$ for Run 6) $t_{v-Run1}/t_{v-Run6}(= (55\text{–}35\,\mathrm{s})/(40\text{–}23\,\mathrm{s}) = 1.2)$ is approximately equal to cube root of the ratio of the buoyancy flux $(B_{-Run6}/B_{-Run1})^{1/3}(= 1.3)$, suggesting that $t_v \sim (H^2/B)^{1/3}$ is the correct time scale for the ring development stage within the current angular velocity range.

### 4.4. *Development of the rim current and generation of the convective cells*

As the convective rings reach the top shelf, a column of convective fluid, which is mainly confined to the volume defined by the heated disk and the top shelf, is formed. Figure 10 shows that the axisymmetric ring structure still holds at $t = 140\,\mathrm{s}$ inside the convective fluid column. At $t = 140\,\mathrm{s}$, small wavy perturbations are observed on some of the convective rings (figure 11). The amplitude of the perturbations grows with time and the rings have broken into cells by $t = 180\,\mathrm{s}$ (figure 12). At this time, an inclined front dividing the heated and ambient fluid has already formed (figure 13*a*). The individual elements of the convective cell consist of an ascending core in the middle surrounded by a cylindrical surface on which descending motions are observed.

One possible explanation of the cause of the breakdown of the rings was given by Boubnov & Golitsyn (1986) as follows. As shown in figure 7, warm fluid moves towards the centre of the ring near the bottom and then rises at the centre of the rings from the bottom of the heated disk. Due to the Coriolis force the fluid at different sides of the rings is deflected in opposite directions causing a shear instability to generate the vortices. However, the present simulation results show that vortices

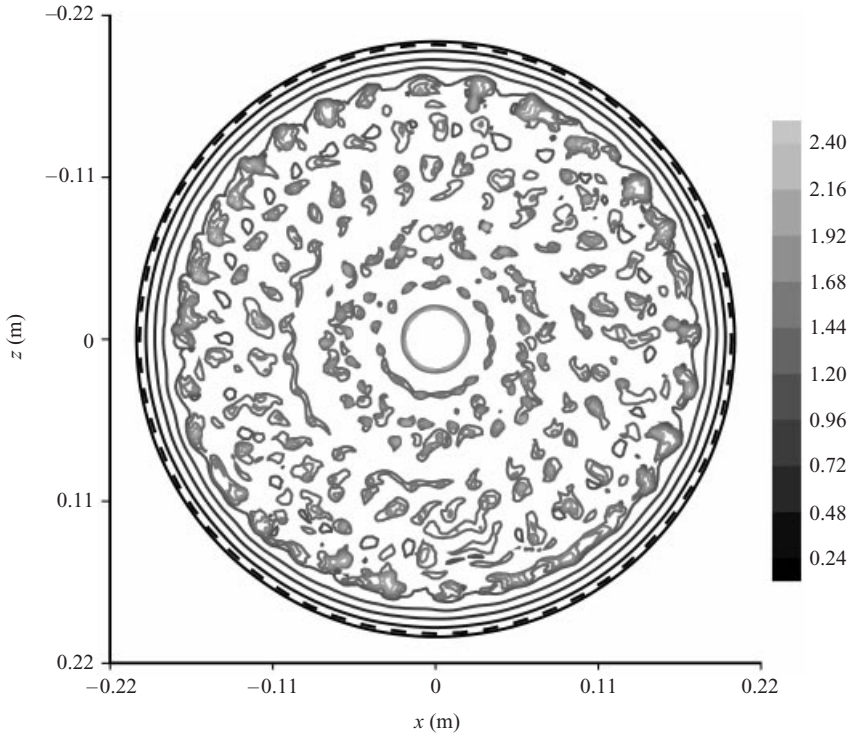


FIGURE 12. As figure 11 but at $t = 180$ s.

are formed with or without rotation. Without rotation, the rings are breaking into vortices by $t = 90$ s as opposed to $t = 140$ s when rotation is present. Thus, the above explanation is not satisfactory, nor as mentioned by Boubnov & Golitsyn (1986) is it the only possible cause. In this early stage, the exact geometry does not have any influence on the development of the convective cells, and this is confirmed by both the experiments of Jacobs & Ivey (1998, 1999), although these authors only showed this early stage of their experiment in the flat lid case (Jacobs & Ivey 1999). One possible reason for the more rapid breakdown of the rings to the individual cells in the experiment is that the conditions in the laboratory experiment are not as ideal as in our numerical simulation, e.g. a uniformly heated disk is hard to maintain in the experiment since the hot water used to heat the disk was pumped in from outside in a radial flow at time $t = 0$.

Unlike in Boubnov & Golitsyn's (1986) experiment, in our simulation all of the rings appear at the same time and grow at the same rate except near boundaries of the convective region, which was confirmed by the experiment done by Coates & Ivey (1993). Their experiment is similar to our simulation's corresponding experiment (Jacobs & Ivey 1998). While the exact geometry may not affect the early development of the rings, the boundary conditions in Boubnov & Golitsyn's (1986) experiment are different from those in our simulation and Jacobs & Ivey's (1998) experiments. Specifically, in Boubnov & Golitsyn's (1986) experiment, the heat flux was applied to the entire bottom of the tank and the sidewalls of the tank were thermo-insulated, while in Jacobs & Ivey's (1998) experiment and our simulation, the heat flux was only applied to a centred circular area with diameter only 42% of the tank diameter and the sidewalls of the tank were maintaned at a constant temperature. This could

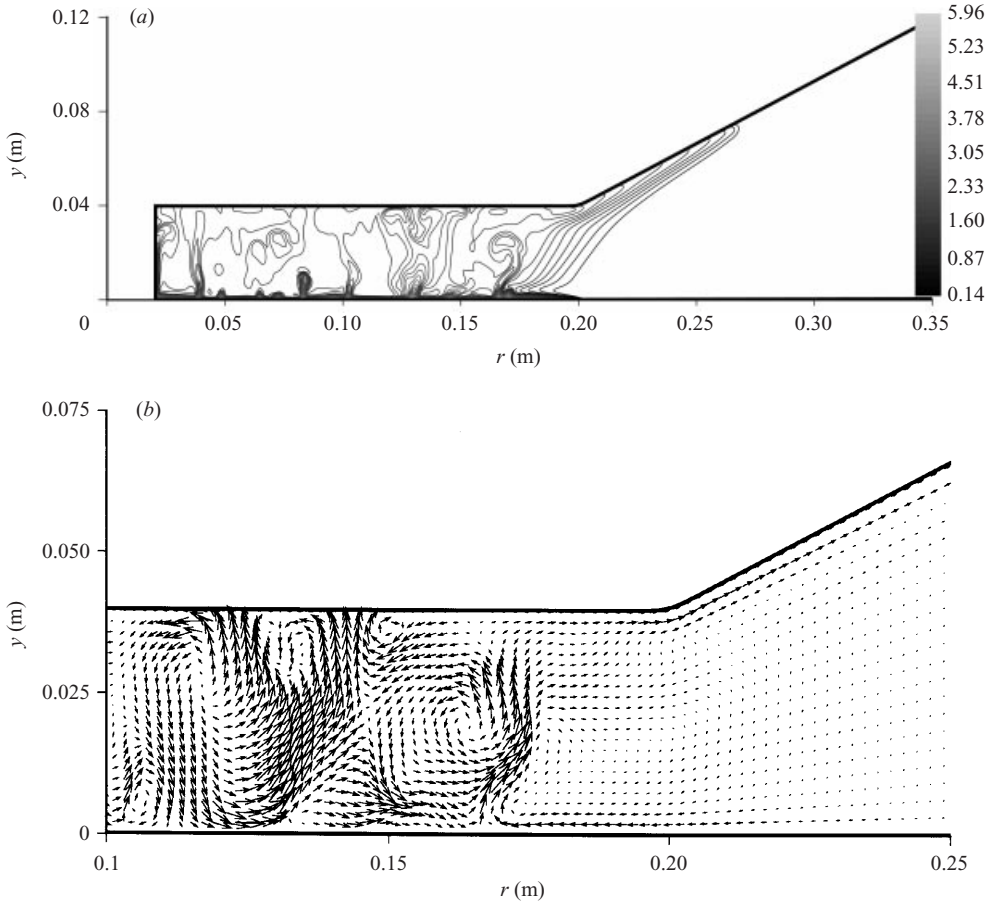


FIGURE 13. Side view of (*a*) temperature field (*b*) expanded velocity field (the maximum velocity magnitude is $3.83\,\mathrm{mm\,s^{-1}}$) at $t = 180\,\mathrm{s}$ for $\Omega = 0.2\,\mathrm{rad\,s^{-1}}$, $B = 1.57 \times 10^{-6}\,\mathrm{m^2\,s^{-3}}$ (Run 1).

be the major contributing factor to the difference observed in the ring development stage between our simulation and Boubnov & Golitsyn's (1986) experiment.

Once the convective fluid reaches the top shelf, it is transported away along the top slope in a thin layer due to the existence of the adjacent slope, and some radial adjustments also occur at the bottom of the tank with colder ambient fluid moving radially in over the heated disk (figure 13*b*).

The horizontal characteristics of the convective cells (vortices) can be seen from the horizontal slices of the velocity field† cut at three different vertical levels ($y/H = 0.125$, 0.5 and 0.875). By $t = 180\,\mathrm{s}$, some small-scale convective vortices are clearly visible at the lower level of the tank ($y/H = 0.125$) (figure 14) above the heated disk. At this level, most of the cells are rotating cyclonically. Outward from the heated disk, there is a quiescent region. Between the two regions, an azimuthal rim current which flows in a cyclonic direction has already developed. The rim current is perturbed by the individual vortices. As explained by Coates *et al.* (1995), the incoming ambient flow at the bottom of the tank must speed up in order to conserve angular momentum

† All the plan view velocity plots in this paper are plotted at every sixth point in the radial direction and at every point in the azimuthal direction.

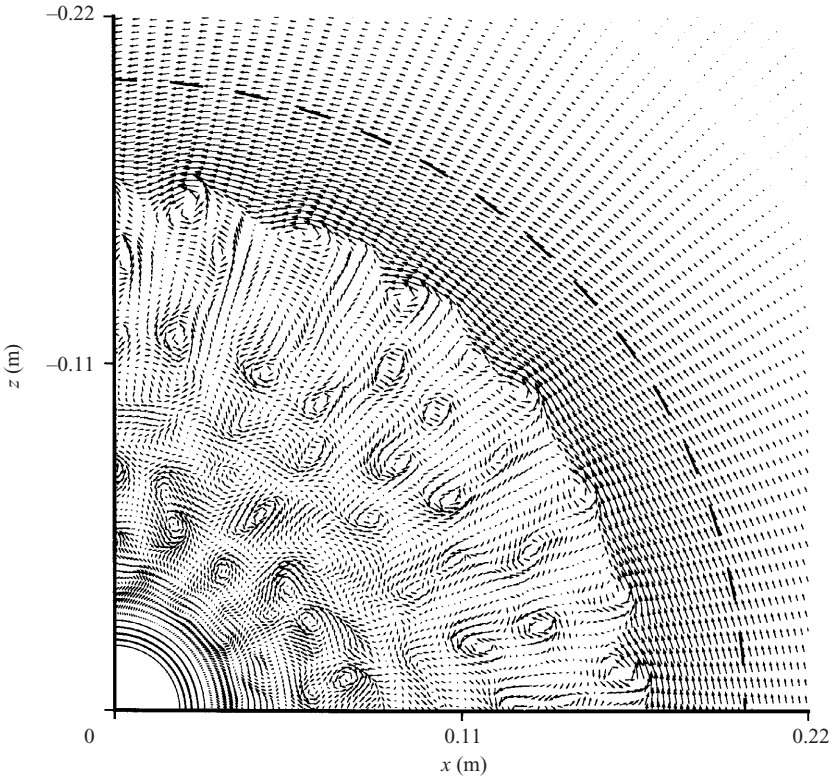


FIGURE 14. Plan view of the velocity field at $t = 180\,\mathrm{s}$ and $y/H = 0.125$ for $\Omega = 0.2\,\mathrm{rad\,s^{-1}}$, $B = 1.57 \times 10^{-6}\ \mathrm{m^2\,s^{-3}}$ (Run 1). The maximum velocity magnitude is $5.68\,\mathrm{mm\,s^{-1}}$. The rim of the heated disk is marked by the dashed line.

and hence acquires a cyclonic rotation. The opposite is true for the rim current at the upper level of the tank. Figure 15 shows that the rim current at the upper level ($y/H = 0.875$) indeed flows in the anti-cyclonic direction. Since the rim current is caused by the system rotation and the conservation of angular momentum, no rim current should develop when there is no rotation, which is confirmed by our simulation result of Run 2 ($\Omega = 0$). Figure 15 also shows that the outlines of the individual convective cells at the upper level are not as clear as those at the lower level and the vortices now have no preferred direction of rotation. As pointed out by Nakagawa & Frenzen (1955), the direction of the horizontal circulation of each cell is that appropriate to the conservation of angular momentum in the divergent or convergent field. At the mid-height of the tank (not shown here), there is no distinct rim current and only the general outline of the convective cells can be seen.

By computing the rim current velocity $u_{\mathrm{rim}}$ at $t = 150\,\mathrm{s}$ and $200\,\mathrm{s}$ for Run 1 and $t = 200\,\mathrm{s}$ for Run 4 and Run 5, we found that the magnitude of $u_{\mathrm{rim}}$ is proportional to $t^{1/2}/f^{3/2}$. Since the buoyancy flux $B$ is the same for Runs 1, 4 and 5, a dimensionally correct velocity scale for $u_{\mathrm{rim}}$ can be as follows:

$$u_{\mathrm{rim}} \sim \frac{Bt^{1/2}}{Hf^{3/2}}. \tag{4.6}$$

We did not compute rim current velocity beyond $t = 200\,\mathrm{s}$ due to the distortion of the rim current caused by the baroclinic instability at later times. The rim current

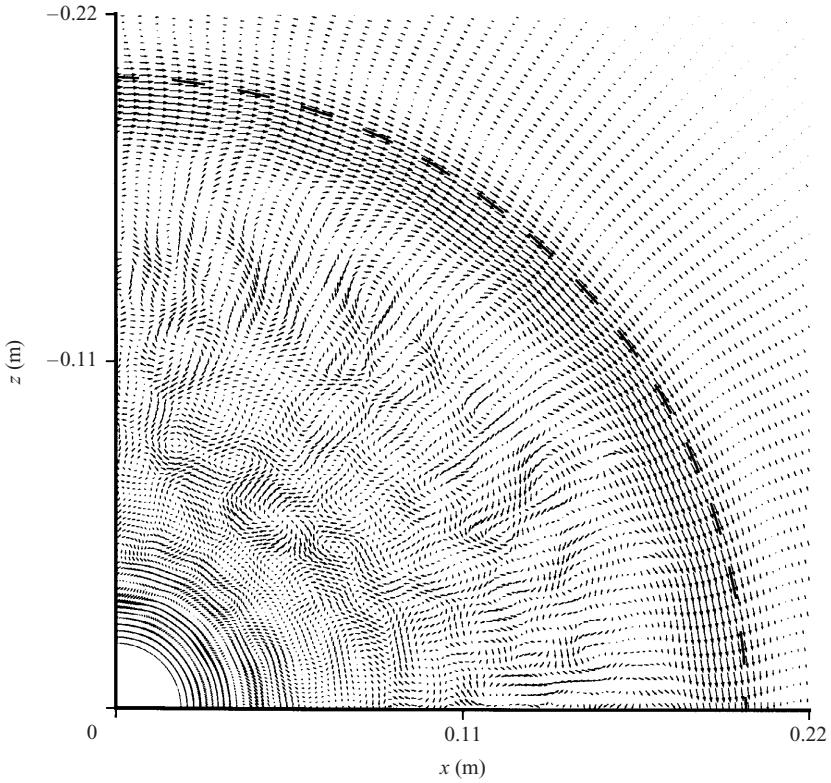


FIGURE 15. As figure 14 but at $y/H = 0.875$. The maximum velocity magnitude is 3.97 mm s$^{-1}$.

generated around the periphery of the heated disk must be in thermal wind balance with the density gradient between convective and ambient regions:

$$f\frac{\partial u_{\rm rim}}{\partial y} \sim \frac{\partial g'}{\partial r}, \tag{4.7}$$

where $y$ and $r$ are the vertical and radial coordinates, $f$ is the Coriolis parameter and $g' = g\Delta\rho/\rho = g\beta\Delta T = Bt/H$ is the reduced gravity resulting from heating from the bottom with the buoyancy flux $B$ for a time $t$ and mixing the column over the depth $H$. Following Send & Marshall (1995), the width of the rim current $L_{\rm rim}$ is $R_D/(2\pi Ro^*)$ based on the $g' = Bt/H$ at the time considered. Applying thermal wind balance (4.7) to a vertical shear of $u_{\rm rim}$ over a vertical depth of $H/2$ (our simulation results show the rim current goes to zero or reverses at mid-depth) yields

$$u_{\rm rim} \sim \frac{1}{2}\frac{g'H}{fL_{\rm rim}} = \frac{\pi Bt^{1/2}}{Hf^{3/2}}. \tag{4.8}$$

The above scaling (see also Send & Marshall 1995) is the same as that found from our simulation results (4.6).

The merging of convective cells is evident from the velocity field at $t = 200$ s and the along-front wave-like instability appears to grow with time (figure 16). By $t = 200$ s, the horizontally axisymmetric flow pattern (figure 10) has fully evolved into a quasi-two-dimensional irregular vortex field (figure 17). A similar evolution process from convective rings to convective cells was also observed in the experiments of Boubnov & Golitsyn (1986). At this stage, the basic determining parameters are

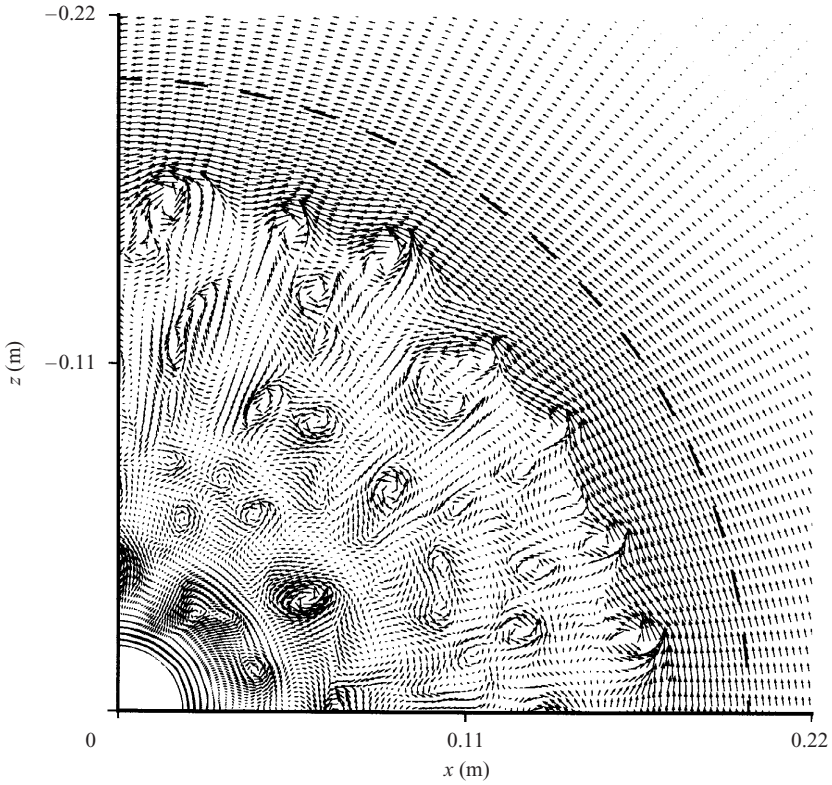


FIGURE 16. As figure 14 but at $t = 200$ s. The maximum velocity magnitude is 7.10 mm s$^{-1}$.

the Rayleigh flux number $Ra_f = BH^4/\kappa^2 v$ and Taylor number $Ta$. Since the fluid confined to the volume defined by the heated disk and the top shelf is all convected, the total depth $H$ should be used to replace the thermal layer thickness $\delta$ in equation (4.4). The pair of $Ra_f$ and $Ta$ values ($Ta = 4 \times 10^5$ and $Ra_f = 2 \times 10^8$) put Run 1 in the irregular geostrophic turbulence regime among the regimes diagram presented in Boubnov & Golitsyn (1990). Figures 16 and 17 show the irregular vortex convection pattern.

### 4.5. *Development of the baroclinic instability*

As mentioned before, the rim current is already perturbed by individual vortices by $t = 180$ s (figure 14). The horizontal temperature difference between the convective and ambient regions continuously increases with time as heat is being added constantly to the system until a steady state is reached within the convective region. The lateral temperature (density) difference increases with time, and so does the available potential energy. This available potential energy is the energy source for baroclinic instability (cf. Jacobs & Ivey 1998). Therefore, with increasing lateral temperature gradient the rim current undergoes a baroclinic instability, which is triggered by the individual vortices of the convective flow. A steady state is reached when all the heat added from the bottom heated disk leaves the convective region through the action of the baroclinic eddies around the periphery of the convective region. As shown in the velocity fields (figures 16, 18 and 19), the instability grows in amplitude with time, while the number of baroclinic eddies formed around the edge of the heated disk decreases with time. Figure 18 shows that each baroclinic vortex is made up of a

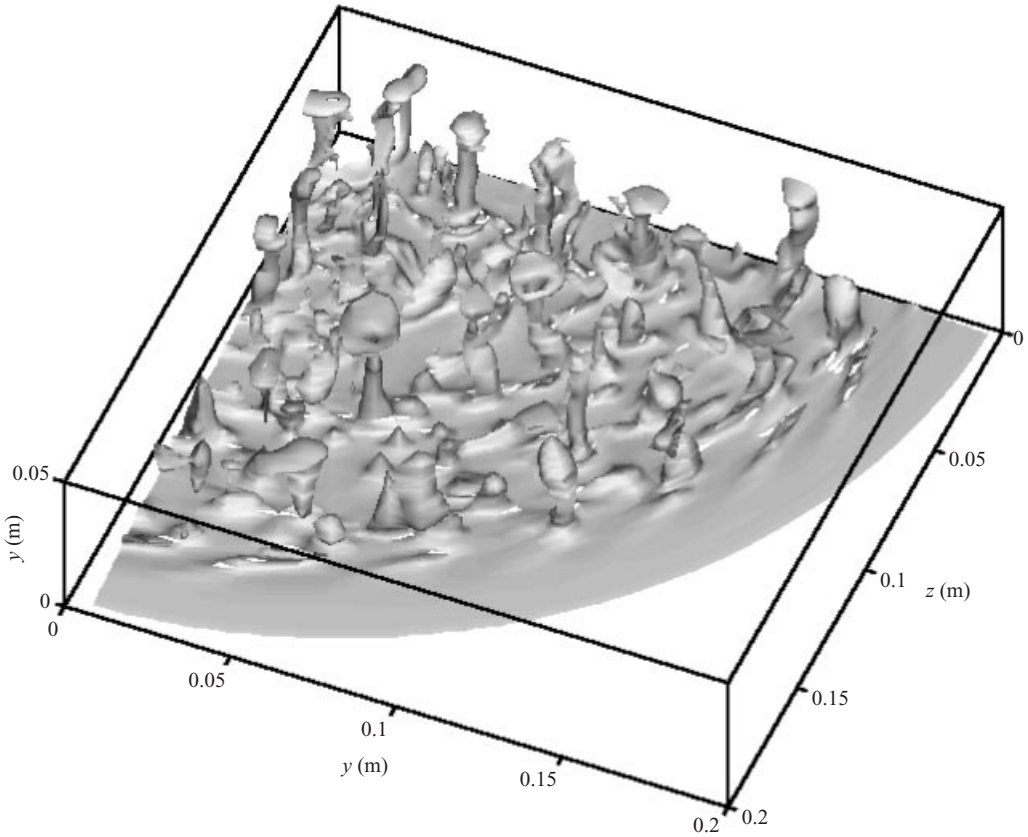


FIGURE 17. An iso-thermal surface at $t = 200\,\mathrm{s}$ for $\Omega = 0.2\,\mathrm{rad\,s^{-1}}$, $B = 1.57 \times 10^{-6}\,\mathrm{m^2\,s^{-3}}$ (Run 1).

number of individual convective cells. This vortex structure was also confirmed by the experimental study of Maxworthy & Narimousa (1994). Because the convective cells coalesce with time, the baroclinic eddies reduce in number and grow in amplitude. All the baroclinic eddies observed are cyclonic eddies. The shapes of the eddies are somewhat different at different vertical levels, *i.e.* the eddies at the lower level have narrow heads (figure 19) and the eddies at the higher level have full round heads (figure 20). Strong cyclonic eddies are observed above the slope in the initially quiescent ambient fluid due to the instability of the rim current and the outflow of the warm convective fluid onto the slope. Unlike in the constant-depth tank case (Jacobs & Ivey 1999), in which the baroclinic eddies fill almost the entire working fluid shortly after they formed, the eddies stay close to the shelf break in the present numerical study and in Jacobs & Ivey's (1998) experimental study to conserve the potential vorticity (Nassef 1998).

Continuous temperature time series were obtained at two fixed positions in the tank, i.e. $r/R_i = 0.5$, 0.75 and $y/H = 0.75$. Figure 21 shows that the fluid is well mixed horizontally within the convective region at level $y/H = 0.75$ from early on and therefore there was little horizontal temperature difference between the two radial locations ($r/R_i = 0.5$, 0.75 and $y/H = 0.75$) within the convective region. Figure 22 compares the temperature time history obtained by numerical simulation at two points with the same radial location with an angular separation of 90° ($r/R_i = 0.75$

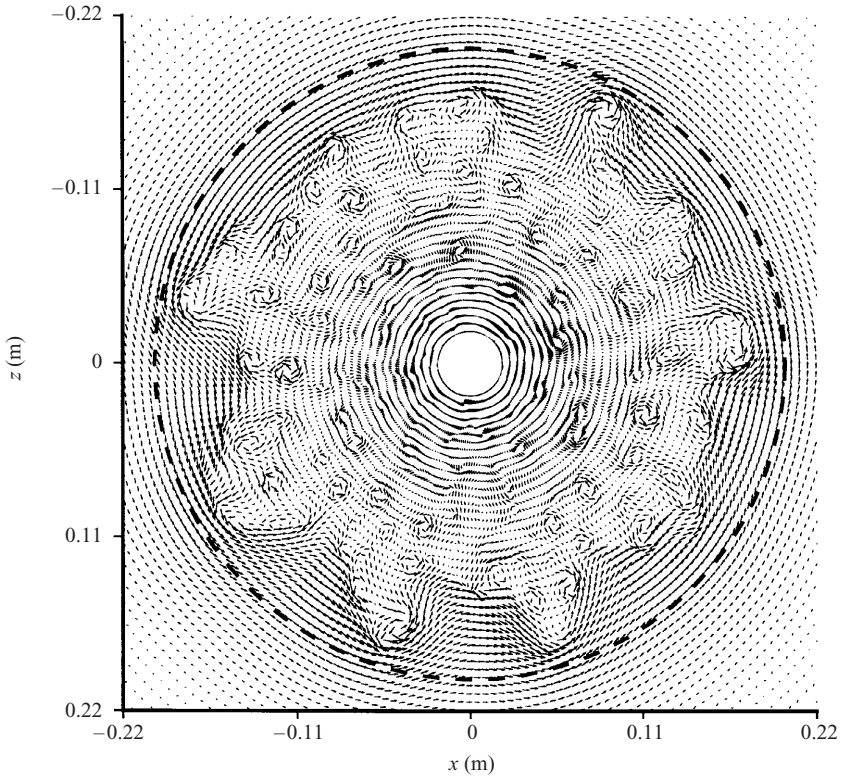


FIGURE 18. Plan view of the velocity field at $t = 240\,\mathrm{s}$ and $y/H = 0.125$ for $\Omega = 0.2\,\mathrm{rad\,s^{-1}}$, $B = 1.57 \times 10^{-6}\,\mathrm{m^2\,s^{-3}}$ (Run 1). The maximum velocity magnitude is $8.68\,\mathrm{mm\,s^{-1}}$. The rim of the heated disk is marked by the dashed line.

and $y/H = 0.75$) with the experimental data collected at the same radial location ($r/R_i = 0.75$ and $y/H = 0.75$) by Jacobs & Ivey (1998). The spike between 100 s and 120 s in the experimental data might be caused by uncertainty in plate heating in the experiment since there is no apparent reason for the temperature field to fluctuate in such a manner during that time. Otherwise, the simulation result follows the trend of the experimental data well. For times beyond 280 s when the baroclinic instability arises, the differences between the experimental data and simulation results or between the simulation results at same radius but different angular locations are simply due to the fact that the experimental probes and the simulation probes were located at the different parts of the baroclinic eddies at a given time.

By the comparison of the horizontal velocity fields at the same level for two different rotating rates (Run 1 and Run 4), it is clear that the size of the baroclinic eddies depends on the rotation rate $\Omega$ of the system. The wavelength $\lambda$ of the baroclinic eddies is found to be a function of the Rossby deformation radius $R_D$ (Jacobs & Ivey 1998), which is given by

$$R_D = \frac{\sqrt{g'H}}{2\Omega}, \tag{4.9}$$

where $g' = g\beta\Delta T$ is the reduced gravity, $\beta$ is the thermal expansion coefficient, $\Omega$ is the system rotation rate, and $H$ is the distance between the tank bottom and the top shelf.

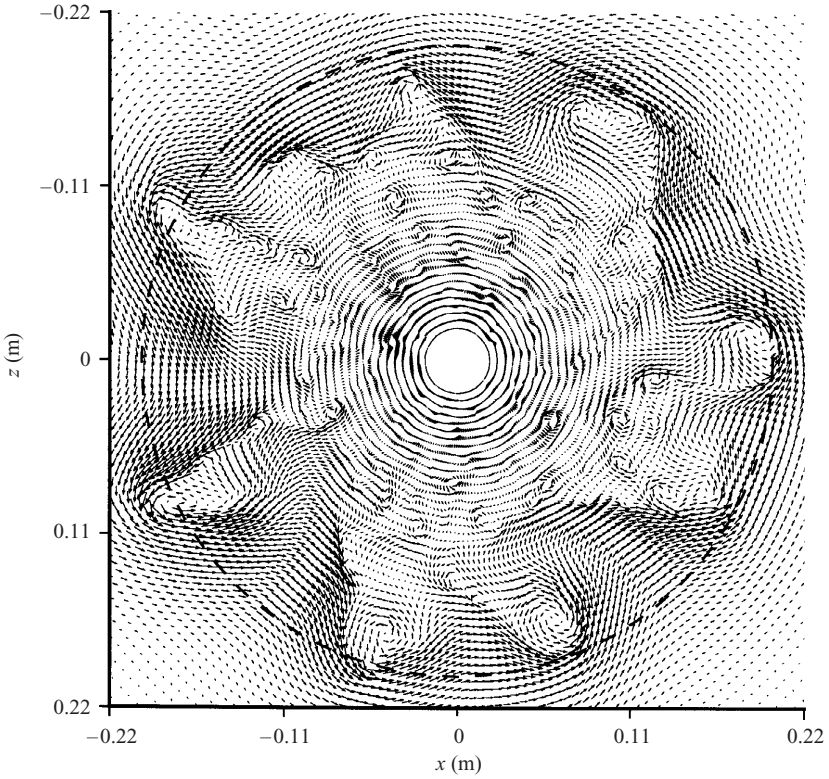


FIGURE 19. As figure 18 but at $t = 280$ s. The maximum velocity magnitude is 10.2 mm s$^{-1}$.

To obtain the steady-state time $\tau$, Jacobs & Ivey (1998) ran each of their experiments for a long time and then estimated the time for steady state from the time series of temperature measurements. Based on all the experiments they performed, they deduced a steady-state time scale as

$$\tau = (3.1 \pm 0.5)(f/B)^{1/2} R_i. \tag{4.10}$$

Since we could not afford to run our simulations to a time that is longer than $\tau$, we used the formula provided by Jacobs & Ivey (1998) (4.10) to estimate $\tau$ in our simulation. For Run 1 and Run 4, the estimated steady-state time is between 260 and 350 s and 370 and 500 s, respectively. Therefore, we run our simulations to 350 s and 500 s for Run 1 and Run 4, respectively. The number of baroclinic eddies observed by Jacobs & Ivey (1998) was six for Run 1 at the steady-state phase of their experiment. There appear to be six baroclinic eddies formed around the rim of the heated disk (figure 23) at $t = 350$ s for Run 1 as well and the number of eddies was unchanged since $t = 320$ s. The average temperature increase within the convective region is 2.4 °C at $t = 350$ s for Run 1, which is within the range of the average temperature increase (2.56 °C ± 0.47 °C) at the steady-state phase of the corresponding experiment (Jacobs & Ivey 1998). Thus, a correlation between the wavelength of the baroclinic eddies and the Rossby deformation radius $R_D$ was obtained as $\lambda = 5.5R_D$ for Run 1. For Run 4, ten baroclinic eddies and an average temperature increase of 2.75 °C within the convective region were found at $t = 500$ s, which leads to a correlation of $\lambda = 6.1R_D$. The correlation constants $C_\lambda$ found by present study (5.5 and 6.1) fall within the experimental range of Brickman (1995), who found a constant of 5.7 ± 0.9.

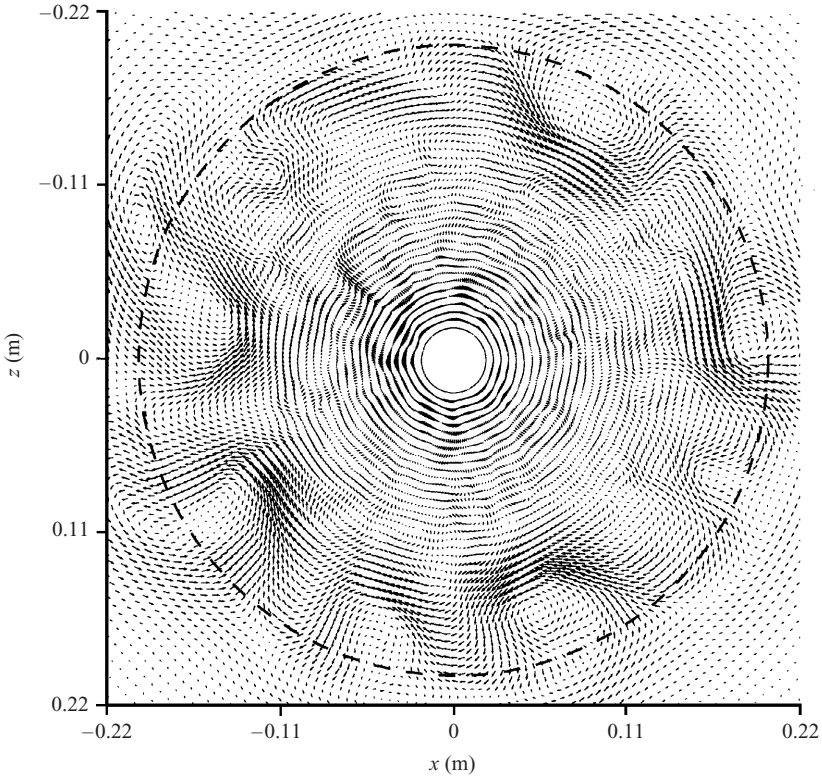


FIGURE 20. As figure 18 but at $t = 280\,\mathrm{s}$ and $y/H = 0.875$. The maximum velocity magnitude is $8.09\,\mathrm{mm\,s^{-1}}$.

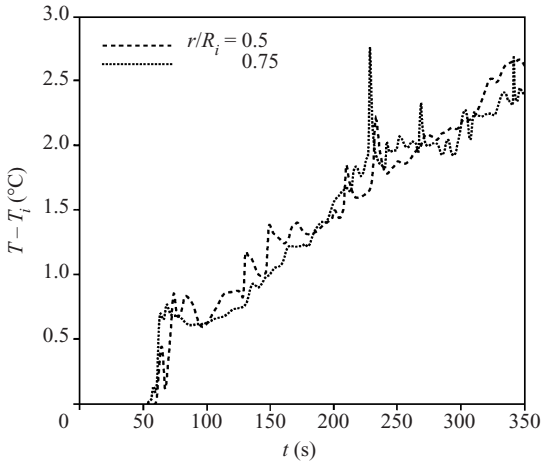


FIGURE 21. Temperature time history at $y/H = 0.75$ for $\Omega = 0.2\,\mathrm{rad\,s^{-1}}$, $B = 1.57 \times 10^{-6}\,\mathrm{m^2\,s^{-3}}$ (Run 1).

Our results are in reasonable agreement with the experimental result of Jacobs & Ivey (1998), who reported a constant of $5.9 \pm 0.3$.

There are conflicting results regarding whether the density anomaly between the convective and ambient regions depends on the system rotation rate. Brickman

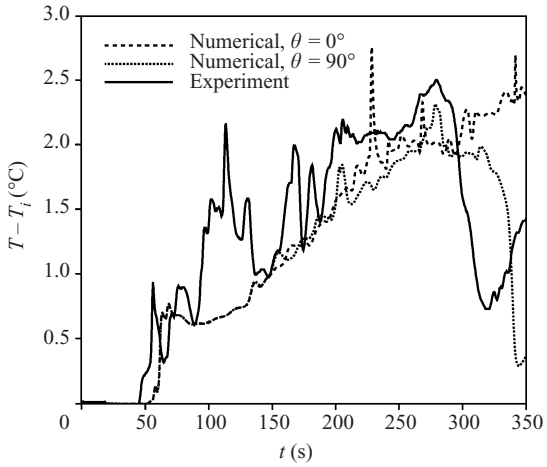


FIGURE 22. Temperature time history at $y/H = 0.75$ and $r/R_i = 0.75$ for $\Omega = 0.2\,\mathrm{rad\,s^{-1}}$, $B = 1.57 \times 10^{-6}\,\mathrm{m^2\,s^{-3}}$ (Run 1).

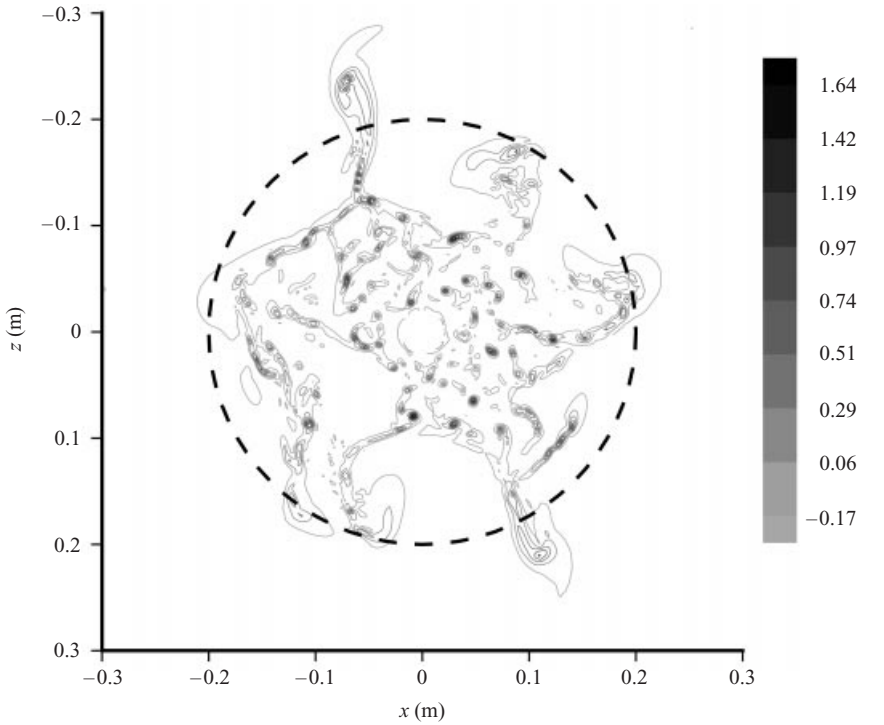


FIGURE 23. Plan view of the vertical vorticity field at $t = 350\,\mathrm{s}$ and $y/H = 0.125$ for $\Omega = 0.2\,\mathrm{rad\,s^{-1}}$, $B = 1.57 \times 10^{-6}\,\mathrm{m^2\,s^{-3}}$ (Run 1). The rim of the heated disk is marked by the dashed line.

(1995) and Narimousa (1997) reached the conclusion that the final density anomaly is independent of the background rotation in a constant depth ocean. However, Jones & Marshall (1993), Chapman & Gawarkiewicz (1997) and Jacobs & Ivey (1998) all found such a dependence. When the rotation rate increases, lateral heat exchanges are more restrained at higher rotation rate as a result of the more restrained radial

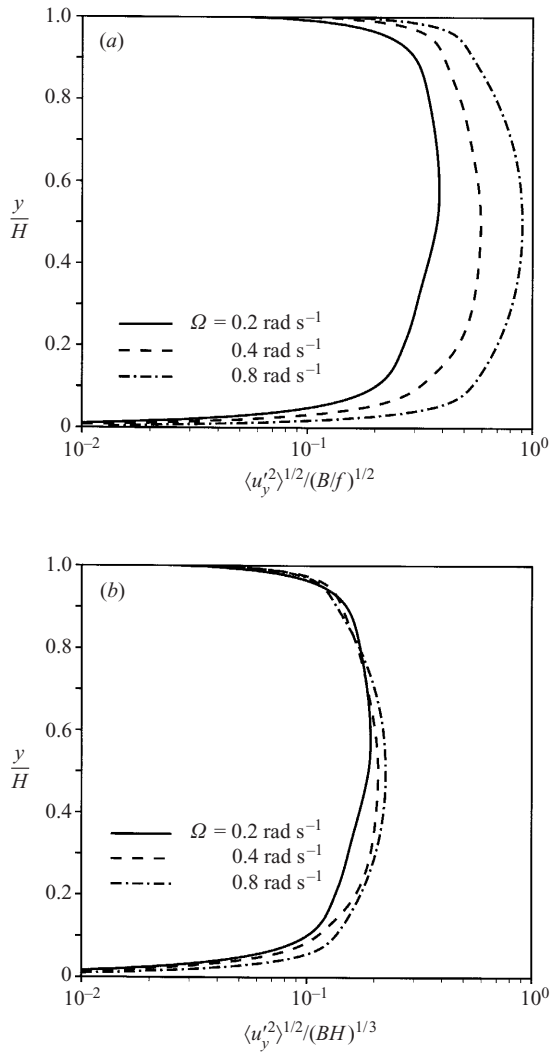


FIGURE 24. Vertical r.m.s. velocity $\langle u_y'^2\rangle^{1/2}$ at $t = 320\,\mathrm{s}$ for Run 1 ($\Omega = 0.4\,\mathrm{rad\,s^{-1}}$), Run 4 ($\Omega = 0.4\,\mathrm{rad\,s^{-1}}$) and Run 5 ($\Omega = 0.8\,\mathrm{rad\,s^{-1}}$): (*a*) non-dimensionalized with the rotational scale $(B/f)^{1/2}$; (*b*) non-dimensionalized with the non-rotational scale $(BH)^{1/3}$.

momentum exchanges between the convective and ambient fluid. We found that the averaged temperature increase within the convective region for Run 4 ($\Omega = 0.4\,\mathrm{rad\,s^{-1}}$) is always higher than that of Run 1 ($\Omega = 0.2\,\mathrm{rad\,s^{-1}}$) at the same time. The average temperature increases within the convective region for Run 1 and Run 4 are 2.4 °C at $t = 350\,\mathrm{s}$ and 2.75 °C at $t = 500\,\mathrm{s}$, respectively. Thus the steady-state density anomaly between the convective and ambient regions can be described by the correlation $g' = C_{g'}(Bf)^{1/2}R/H$. The correlation constants $C_g'$ found in our simulations for Run 1 and Run 4 are 1.5 and 1.2, respectively. A correlation constant of $(1.6 \pm 0.2)$ was found by the experimental study of Jacobs & Ivey (1998). Thus, our results reasonably agree with the experiment study of Jacobs & Ivey (1998) and support the dependence hypothesis.

We think that the discrepancies in the above two correlations constants ($C_\lambda$ and $C_{g'}$)

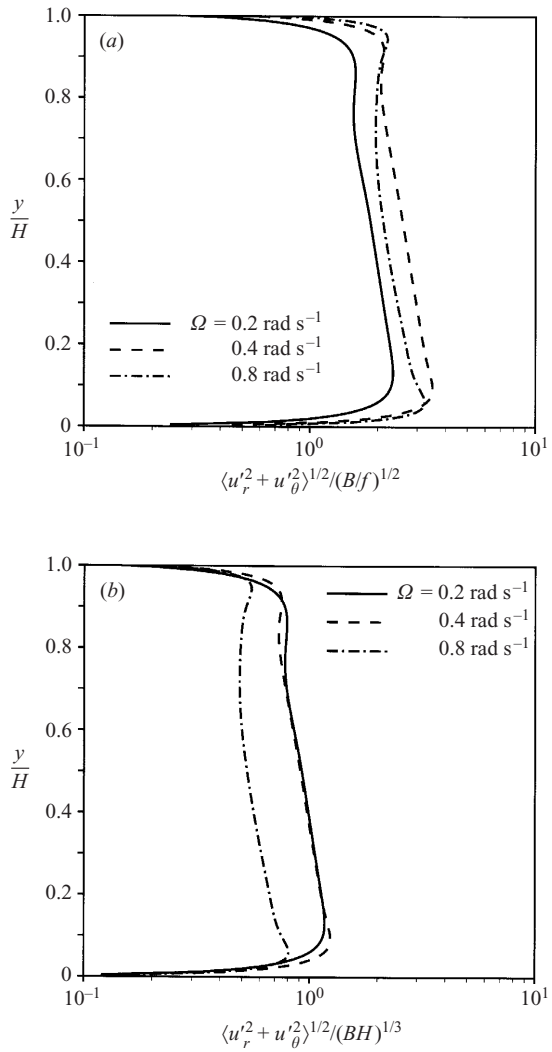


FIGURE 25. Horizontal r.m.s. velocity $\langle u_r'^2 + u_\theta'^2 \rangle^{1/2}$ at $t = 320$ s for Run 1 ($\Omega = 0.2$ rad s$^{-1}$), Run 4 ($\Omega = 0.4$ rad s$^{-1}$) and Run 5 ($\Omega = 0.8$ rad s$^{-1}$): (*a*) non-dimensionalized with the rotational scale $(B/f)^{1/2}$; (*b*) non-dimensionalized with the non-rotational scale $(BH)^{1/3}$.

between the simulation and the experimental results are due to the following facts. First, our simulations were carried out under the same conditions as the experiment except that a small cylinder of radius $R_h = 0.02$ m was cut from the numerical domain to eliminate the coordinate singularity at the centre. Secondly, the averaged temperature within the convective region in our simulation was obtained by taking the average of the temperature of all the computational cells within the convective region, whereas there were only two or four (depends on different experiment runs in Jacobs & Ivey's experiments) probes at fixed radial locations within the convective region in the experiment to measure the temperature. Finally, it is difficult to count the number of baroclinic waves accurately from the highly irregular flow structures obtained, whether in the experiment or numerical simulation, especially when the number of baroclinic waves increased at higher rotation rate.

The effect of rotation on turbulent convection was also investigated. The turbulent root mean square (r.m.s.) horizontal velocity $\langle u_r'^2 + u_\theta'^2 \rangle^{1/2}$ and vertical velocity $\langle u_y'^2 \rangle^{1/2}$ are obtained at a radial location $r/R_i = 0.5$ by averaging the velocity components over the azimuthal direction. Spatial averaging is denoted by $\langle\ \rangle$ and $u_i' = u_i - \langle u_i \rangle$. Figures 24(*a*) and 24(*b*) plot the vertical r.m.s. velocity non-dimensionalized with both the rotational velocity scale $(B/f)^{1/2}$ and the non-rotational velocity scale $(BH)^{1/3}$ as a function of the depth over the heated disk at $t = 320\,\mathrm{s}$ for Runs 1, 4 and 5. We found that the vertical velocity scales better with the non-rotational scaling. This finding is consistent with that of Boubnov & Golitsyn (1990).

Figures 25(*a*) and 25(*b*) in which horizontal r.m.s. velocity non-dimensionalized by the two velocity scales is plotted against the depth show that non-rotational scaling gives a better description of the convective turbulence for Run 1 ($\Omega = 0.2\,\mathrm{rad\,s^{-1}}$) and Run 4 ($\Omega = 0.4\,\mathrm{rad\,s^{-1}}$). With the rotation rate further increased, Run 4 ($\Omega = 0.4\,\mathrm{rad\,s^{-1}}$) and Run 5 ($\Omega = 0.8\,\mathrm{rad\,s^{-1}}$) scale better with the rotational velocity scale, suggesting that there is a transition from the buoyancy-flux-controlled flow to background-rotation-controlled flow. The natural Rossby number gives a measure of the importance of rotation on the convective process. A critical value of $Ro^*$ marks the transition from the regime in which buoyancy flux controls the small-scale convective turbulence to the regime in which background rotation controls the convective turbulence. From table 1, the natural Rossby number $Ro^*$ for Runs 1, 4 and 5 are 0.124, 0.044 and 0.015, respectively. Some experimental estimates of the critical value of $Ro^*$ vary over almost one order of magnitude. Fernando *et al.* (1991) found $0.03 \leqslant Ro^* \leqslant 0.22$, while Coates & Ivey (1997) indicated $0.02 \leqslant Ro^* \leqslant 0.05$. Our simulation result suggests that $0.015 \leqslant Ro^* \leqslant 0.044$, which agrees with the finding of Coates & Ivey (1997) but further narrows down the range of the critical value of $Ro^*$.

## 5. Conclusions

This study provides a step-by-step precise description and investigation of the development of a turbulent rotating convective flow. The present simulations were able to show for the first time the detailed temporal evolution and rich spatial structure of the three-dimensional convective flow field on the smallest resolvable scales. Because the large-eddy simulation is carried out under the same conditions as an experiment (Jacobs & Ivey 1998), a direct comparison between the simulation results and the experiment measurements can be made. All of our six simulation runs (table 1) confirmed Jacobs & Ivey's finding that the convective overturning time scale $t_v$ is independent of system rotation $\Omega$ as $t_v \sim (H^2/B)^{1/3}$ from (4.5). For example, a heat flux of $300\,\mathrm{W\,m^{-2}}$ will cause convection to reach 200 m in about 2 hours. Six baroclinic eddies were reported by Jacobs & Ivey (1998) for their experiment number 14. About six baroclinic eddies were also observed by our corresponding simulation Run 1 (figure 23). At the steady state, the average temperature difference between the convective and the ambient regions obtained from our simulation was 2.4 °C for Run 1, which is within the range of the average temperature increase (2.56 °C ± 0.47 °C) of the corresponding experiment. The wavelength of the baroclinic eddies at steady state relates to the Rossby deformation radius as $\lambda = C_\lambda R_D$. The correlation constants $C_\lambda$ obtained in this study are 5.5 and 6.1 for Run 1 and Run 4, while the range of the correlation constant found by Jacobs & Ivey's experiments was $5.9 \pm 0.3$. The steady-state density anomaly between the convective and ambient regions can be described by the correlation $g' = C_{g'}(Bf)^{1/2}R/H$. The correlation

constants $C_{g'}$ obtained is this study are 1.5 and 1.2 for Run 1 and Run 4, respectively. A correlation constant of $(1.6 \pm 0.2)$ was found by the experimental study of Jacobs & Ivey (1998).

The objective of this study was not only to compare with but also to complement the experimental study of Jacobs & Ivey (1998) in investigating the fundamental mechanisms of a turbulent rotating convective flow. Our three-dimensional numerical simulations allow us to extract rich information which cannot be easily obtained from laboratory experiments. The following conclusions are drawn from our simulations results and are supported qualitatively or quantitatively by various experimental, theoretical and numerical studies beyond the experimental study of Jacobs & Ivey (1998).

Initially, a basic static state of heat conduction exists within a thin thermal layer – the conductive layer. A correct length scale for the thickness of the conductive layer is $\delta(t) \sim \sqrt{\kappa t}$. When the temperature increase across the conductive layer exceeds a critical value, the basic static state becomes unstable and Rayleigh–Bénard convection is observed through the formation of circular concentric convective rings. The time for the formation of the convective rings is determined only by the supplied buoyancy flux $B$ when $Ta_\delta < 5 \times 10^3$ and begins to increase when $Ta_\delta > 5 \times 10^3$. The number of rings formed depends on the buoyancy flux and the number of rings starts to increase when $Ta_\delta > 5 \times 10^3$. The critical Rayleigh number $Ra_c$ is essentially constant ($Ra_c \approx 7 \times 10^4$) when $Ta_\delta < 5 \times 10^3$ and begins to increase with $Ta_\delta$ as $Ta_\delta > 5 \times 10^3$.

The horizontally axisymmetric ring pattern eventually breaks down and evolves into a quasi-two-dimensional vortex field. A rim current develops around the periphery of the heated disk and is in thermal wind balance with the density gradient between convective and ambient regions. Our simulation results confirmed that the rim current velocity scales as $Bt^{1/2}/Hf^{3/2}$. The rim current later becomes unstable to baroclinic instability and baroclinic waves are observed. The effect of rotation on turbulent convection was also investigated. The turbulent velocities are calculated for three different rotation rates, i.e. $\Omega = 0.2$, 0.4 and $0.8\,\mathrm{rad\,s^{-1}}$. The vertical r.m.s. velocities always scale better with the non-rotating velocity scale. The non-rotational velocity scale can be used to scale the horizontal velocities for lower rotation rates. As the rotation rate further increases, the horizontal r.m.s. velocities scale better with the rotational scaling, indicating that there is a transition from the buoyancy-flux-controlled flow to background-rotation-controlled flow. Our simulation results suggest that this transition point occurred when the natural Rossby number $Ro^*$ became smaller than a critical value between 0.015 and 0.044.

Finally, several questions remain unanswered. The precise nature of the mechanism that causes the breakdown of the convective rings and the formation of the individual convective cells is unclear. In the turbulent rotating convective flow, the density anomaly is thought to depend on the ratio $R_i/H$ of the radius of the heated disk to the distance between the tank bottom and the shelf. However, it is difficult to create an aspect ratio $R/H$ larger than 5–8 in the existing rotating convective flow laboratory setup. Thus, it would be desirable to explore the case for $R_i/H > 10$ numerically and to determine the dependence of the density anomaly on the ratio $R_i/H$ in future work. The effect of changing the bottom slope on the size of the baroclinic eddies could also be investigated by numerical simulations.

The authors are very grateful to Professor Greg Ivey and Dr Pieter Jacobs for providing the details and results of their experimental work and valuable comments and suggestions about our simulations. We are additionally appreciative of Professor Ivey's

comments, suggestions, and advice regarding an earlier version of this manuscript. We thank the three referees for carefully reading our manuscript and making a number of valuable suggestions. We also gratefully acknowledge the computing time on the IBM SP2 provided by NASA Ames and the Cornell Theory Center. The results have been analysed in the Environmental Fluid Mechanics Laboratory at Stanford University. This work was supported by the National Science Foundation through Grant DMS-93181166 (program officer: Dr M. Steuerwalt).

## REFERENCES

Bergeron, R. 1998 Measurement of a scientific workload using the IBM hardware performance monitor. In *10th High Performance Networking and Computing Conference, Orlando, Florida*, SC98 (http://www.supercomp.org/sc98/).

Boubnov, B. M. & Golitsyn, G. S. 1986 Experimental study of convective structures in rotating fluids. *J. Fluid Mech.* **167**, 503–531.

Boubnov, B. M. & Golitsyn, G. S. 1990 Temperature and velocity field regimes of convective motions in a rotating plane fluid layer. *J. Fluid Mech.* **219**, 215–239.

Boubnov, B. M. & Golitsyn, G. S. 1995 *Convection in Rotating Fluids*. Kluwer.

Brickman, D. 1995 Heat flux partitioning in open-ocean convection. *J. Phys. Oceanogr.* **25**, 2609–2623.

Brugge, R., Jones, H. L. & Marshall, J. C. 1991 Non-hydrostatic ocean modeling for studies of open-ocean deep convection. In *Deep Convection and Deep Water Formation in the Oceans* (ed. P. C. Chu & J. C. Gascard), pp. 325–340. Elsevier.

Chandrasekhar, S. 1961 *Hydrodynamic and Hydromagnetic Stability*. Dover.

Chapman, D. C. & Gawarkiewicz, G. 1997 Shallow convection and buoyancy equilibration in an idealized coastal polynya. *J. Phys. Oceanogr.* **27**, 555–566.

Coates, M. & Ivey, G. N. 1993 Instability of a convectively driven mixed layer in a rotating fluid. In *5th Australia Heat Mass Transfer Conference, Sydney, Australia.*

Coates, M. & Ivey, G. N. 1997 On convective turbulence and the influence of rotation. *Dyn. Atmos. Oceans* **25**, 217–232.

Coates, M., Ivey, G. N. & Taylor, J. R. 1995 Unsteady, turbulent convection into a rotating, linearly stratified fluid: Modeling deep ocean convection. *J. Phys. Oceanogr.* **25**, 3032–3050.

Cui, A. 1999 On the parallel computation of turbulent rotating stratified flows. PhD thesis, Department of Mechanical Engineering, Stanford University.

Cui, A. & Street, R. L. 2000 Parallel computing of laboratory-scale realizations of rotating and stratified fluid flows. In *2000 Intl Conf. on Parallel and Distributed Processing Techniques and Applications, Las Vegas, Nevada*, pp. 1423–1429.

Denbo, D. W. & Skyllingstad, E. D. 1996 An ocean large-eddy simulation model with application to deep convection in the Greenland Sea. *J. Geophys. Res.* **101**(C1), 1095–1100.

Fernando, H. J. S., Boyer, D. L. & Chen, R. R. 1989 Turbulent thermal convection in rotating stratified fluids. *Dyn. Atmos. Oceans* **13**, 95–121.

Fernando, H. J. S., Chen, R. R. & Boyer, D. L. 1991 Effects of rotation on convective turbulence. *J. Fluid Mech.* **228**, 513–547.

Garwood, R. W., Isakari, S. M. & Gallacher, P. C. 1994 Thermobaric convection. In *The Polar Oceans and Their Role in Shaping the Global Environment* (ed. O. M. Johannessen, R. D. Muench, & J. E. Overland), vol. 85, pp. 199–207. Geophysical Monograph Series.

Golitsyn, G. S. 1980 Geostrophic convection. *Dokl. Akad. Nauk SSSR* **251**, 1356–1360.

Golitsyn, G. S. 1981 Structure of convection at fast rotation. *Dokl. Akad. Nauk SSSR* **261**, 317–320.

Grötzbach, G. 1982 Direct numerical simulation of laminar and turbulent benard convection. *J. Fluid Mech.* **119**, 27–53.

Hathaway, D. H. & Somerville, R. C. J. 1983 Three-dimensional simulations of convection in layers with tilted rotation vectors. *J. Fluid Mech.* **126**, 75–89.

Jacobs, P. & Ivey, G. N. 1998 The influence of rotation on shelf convection. *J. Fluid Mech.* **369**, 23–48.

Jacobs, P. & Ivey, G. N. 1999 Rossby number regimes for isolated convection in a homogeneous, isolating fluid. *Dyn. Atmos. Oceans* **30**, 149–171.

Jones, H. & Marshall, J. 1993 Convection with rotation in a natural ocean: A study of open-ocean convection. *J. Phys. Oceanogr.* **23**, 1009–1039.

Killworth, P. D. 1983 Deep convection in the world ocean. *Rev. Geophys. Space Phys.* **21**, 1–26.

Klinger, B. A., Marshall, J. & Send, U. 1996 Representation of convective plumes by vertical adjustment. *J. Geophys. Res.* **101**(C8), 18175–18182.

Koschmieder, E. L. 1966 On convection on a uniformly heated plane. *Beitr. Phys. Atmosphäre* **39**, 1–11.

Koschmieder, E. L. 1967 On convection on a uniformly heated rotating plane. *Beitr. Phys. Atmosphäre* **39**, 216–225.

Koschmieder, E. L. 1993 *Bénard Cells and Taylor Vortices*. Cambridge University Press.

Legg, S., Jones, H. & Visbeck, M. 1996 A heton perspective of baroclinic eddy transfer in localized open ocean convection. *J. Phys. Oceanogr.* **26**, 2251–2266.

Legg, S. & Marshall, J. 1993 A heton model of the spreading phase of open-ocean deep convection. *J. Phys. Oceanogr.* **23**, 1040–1056.

Leonard, B. P. 1979 A stable and accurate convective modeling procedure based on quadratic upstream interpolation. *Computer Meth. Appl. Mech. Engng* **19**, 59–98.

Leonard, B. P. 1988 Third order multi-dimensional Euler/Navier-Stokes solver. *AIAA/ASME/SIAM/APS First National Fluid Dynamics Congress*, pp. 226–231.

Madec, G., Chartier, M., Delecluse, P. & Crepon, M. 1991 A three-dimensional numerical model of deep water formation in the northwestern Mediterranean Sea. *J. Phys. Oceanogr.* **21**, 1349–1371.

Maxworthy, T. & Narimousa, S. 1994 Unsteady, turbulent convection into a homogeneous, rotating fluid, with oceanographic applications. *J. Phys. Oceanogr.* **24**, 865–887.

Nakagawa, Y. & Frenzen, P. 1955 A theoretical and experimental study of cellular convection in rotating fluids. *Tellus* **7**(I), 1–21.

Narimousa, S. 1997 Dynamics of mesoscale vortices generated by turbulent convection at large aspect ratios. *J. Geophys. Res.* **102**(C3), 5615–5624.

Nassef, H. R. A. 1998 The effects of rotation on localized buoyancy driven convection. PhD thesis, University of Southern California.

Noh, Y., Jang, C. J. & Kim, J. W. 1999 Large eddy simulation of open ocean deep convection with application to the deep water formation in the East Sea (Japan Sea). *J. Oceanogr.* **55**, 347–367.

Piomelli, U. 1999 Large-eddy simulation: achievements and challenges. *Prog. Aerospace Sci.* **35**, 335–362.

Prasad, A. K. & Koseff, J. R. 1989 Reynolds number and end-wall effects on a lid-driven cavity flow. *Phys. Fluids* A **1**, 208–218.

Raasch, S. & Etling, D. 1991 Numerical simulation of rotating turbulent thermal convection, *Beitr. Phys. Atmosphäre* **64**(3), 185–199.

Rayleigh, Lord 1916 On convection currents in a horizontal layer of fluid when the higher temperature is on the under side. *Phil. Mag.* **32**, 529–546.

Rossby, H. T. 1969 A study of Bénard convection with and without rotation. *J. Fluid Mech.* **36**, 309–337.

Salvetti, M. V. & Banerjee, S. 1995 A priori tests of a new dynamic subgrid-scale model for finite-difference large-eddy simulations. *Phys. Fluids* A **7**, 2831–2847.

Sander, J., Wolf-Gladrow, D. & Olbers, D. 1995 Numerical studies of open ocean deep convection. *J. Geophys. Res.* **100**(C10), 20579–20600.

Schott, F. & Leaman, K. D. 1991 Observations with moored acoustic doppler current profilers in the convection regime in the golfe du lion. *J. Phys. Oceanogr.* **21**, 558–574.

Schott, F., Visbeck, M. & Fischer, J. 1993 Observations of vertical currents and convection in the central greenland sea during the winter of 1988–1989. *J. Geophys. Res.* **98**(C8), 14401–14421.

Send, U. & Marshall, J. 1995 Integral effects of deep convection. *J. Phys. Oceanogr.* **25**, 855–872.

Somerville, R. C. J. & Lipps, F. B. 1973 A numerical study in three space dimensions of Bénard convection in a rotating fluid. *J. Atmos. Sci.* **30**, 590–596.

Visbeck, M., Marshall, J. & Jones, H. 1996 Dynamics of isolated convective regions in the ocean. *J. Phys. Oceanogr.* **26**, 1721–1734.

Yuan, L. L., Street, R. L. & Ferziger, J. H. 1999 Large-eddy simulations of a round jet in crossflow. *J. Fluid Mech.* **379**, 71–104.

Zang, Y. & Street, R. L. 1995 Numerical simulation of coastal upwelling and interfacial instability of a rotating and stratified fluid. *J. Fluid Mech.* **305**, 47–75.

Zang, Y., Street, R. L. & Koseff, J. R. 1993 A dynamic mixed subgrid-scale model and its application to turbulent recirculating flows. *Phys. Fluids* A **5**, 3186–3196.

Zang, Y., Street, R. L. & Koseff, J. R. 1994 A non-staggered grid, fractional step method for time-dependent incompressible Navier-Stokes equations in curvilinear coordinates. *J. Comput. Phys.* **114**, 18–33.